IX. PLASMAS AND CONTROLLED NUCLEAR FUSION

A. Active Plasma Systems*

Academic and Research Staff

Prof. L. D. Smullin
Prof. A. Bers
Prof. R. J. Briggs
Prof. R. R. Parker

Graduate Students

R. R. Bartsch
S-L. Chou
J. A. Davis
F. N. Herba
B. R. Kusse
R. K. Linford
O. Lopez
J. A. Mangano
D. M. Perozek
D. A. Platts
H. M. Schneider
R. N. Wallace

1. SYSTEM C

Introduction

In our last report[1] we discussed the observation of ion-cyclotron waves as generated by modulating the cathode of the electron gun. In this report we present results of exciting ion-cyclotron waves by applying RF voltage to a short coil wound concentric with the plasma column. As in the beam method, the width of the ion resonance is found to be in agreement with our estimate of the effect of ion-neutral collisions, while the damping of the wave is found to be significantly larger than that expected from classical conductivity calculations. We relate the experimental results to the heating problem, outlining a possible procedure for optimally heating a plasma by using ion-cyclotron resonance.

Observation of Ion Cyclotron Waves Generated by a Coil

In our experiment, the output of an RF oscillator was applied to an electrostatically shielded coil consisting of 11 turns of No. 14 Cu wire concentric with the plasma column. The coil itself is shown in Fig. IX-1 and the preparation of the system for these measurements is shown in Fig. IX-2. The plasma response was observed by sliding a magnetic probe inside the 7-mm O. D. Pyrex tube inserted into the system along the axis.

Data for this experiment were obtained by applying the signal developed across the probe to a series LC circuit that filtered and amplified it. The output was displayed simultaneously on two oscilloscopes (Tektronix Type 545, Type H plug-ins), one being used for amplitude measurements, the other for phase. The sweep of both oscilloscopes

*This work was supported by the National Science Foundation (Grant GK-1165).

was synchronized to the oscillator current and the cathode-ray tubes were pulsed on for 100 μsec at a preselected time during the beam pulse. Since the unblanking pulse was

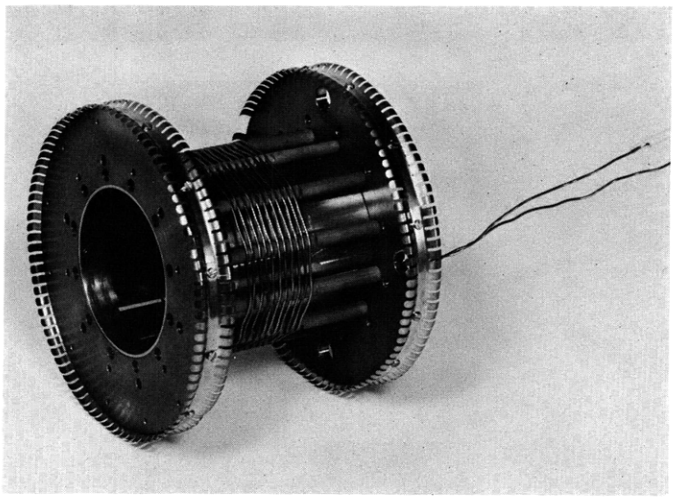

Fig. IX-1. Coil used to excite ion-cyclotron waves.

long compared with the period of the radiofrequency, the signal appearing on the face of the oscilloscopes during each beam pulse was essentially a local time average of the probe signal. After observing the results of several beam pulses, each data point (amplitude and phase) was recorded.

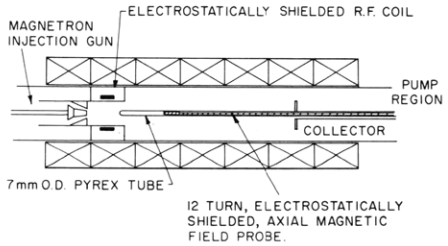

Fig. IX-2. Preparation of the system for coil excitation of ion-cyclotron waves.

A typical set of oscillograms taken at various axial positions in the discharge is shown in Fig. IX-3. Two features are evident, the decay in amplitude vs distance, and a nearly linear phase increase. By making several runs such as this we may obtain plots of the amplitude and phase as functions of distance from the coil. Plots of this sort for several frequencies are shown in Fig. IX-4, where we have plotted the logarithm of the amplitude in anticipation of exponential behavior.

For f = 3.2 MHz and 3.4 MHz, the data indicate the presence of a single wave launched from the coil. For f = 2.8 MHz and 3.0 MHz, on the other hand, there appears

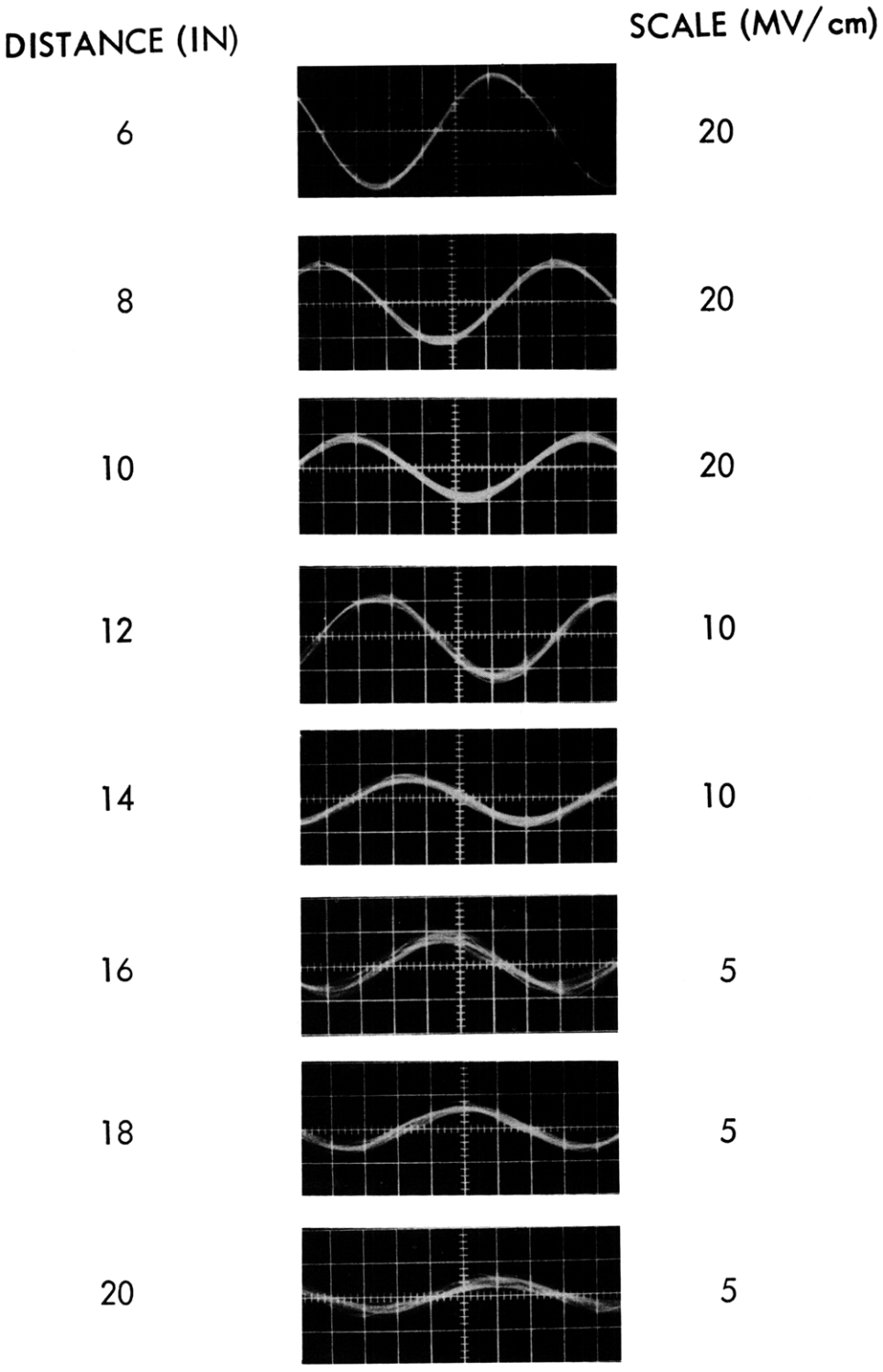

Fig. IX-3. Oscillograms of the coil signal vs time, with distance as parameter.

to be an interfering signal which we believe is due to reflection from the collector. While the magnitude of the reflection coefficient may be less than unity, the position of the first minimum indicates that the collector acts more as an open circuit than a short circuit. This follows because, at a phase of $\pi/2$ from

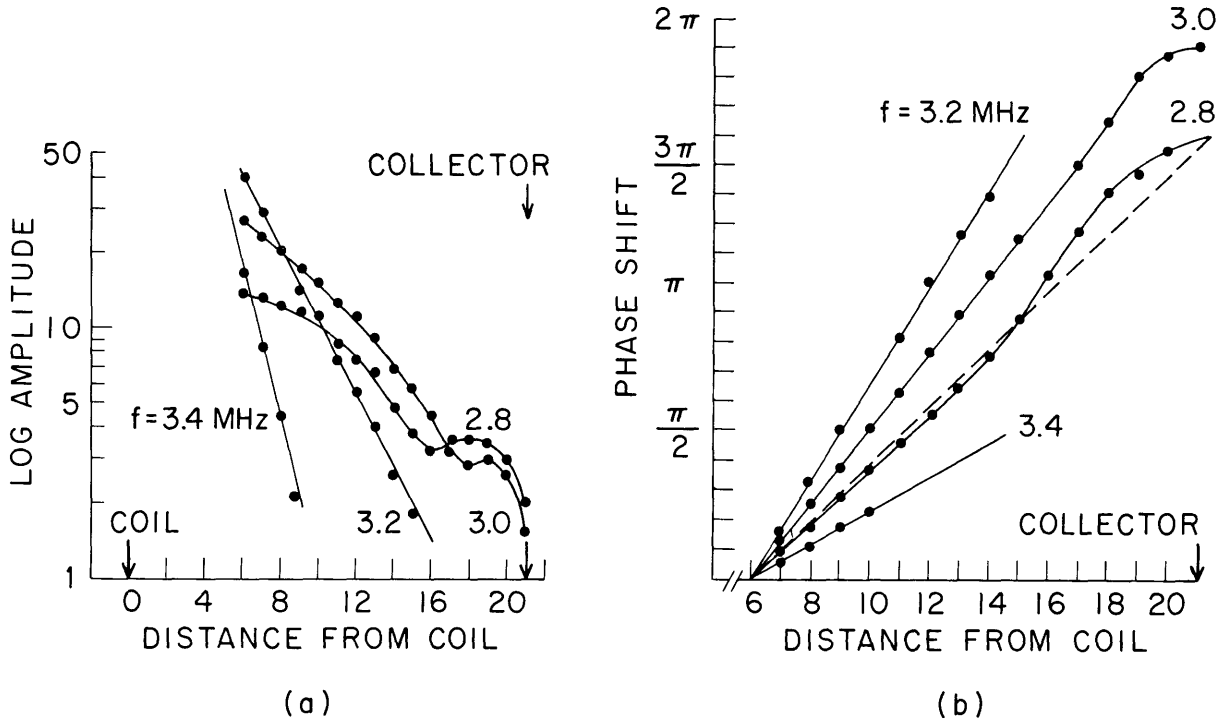

Fig. IX-4. Amplitude and phase of signal resulting from coil excitation vs distance for 4 frequencies (f_{ci} = 3.3 MHz). (a) Log of amplitude vs distance from the coil. (b) Phase vs distance from the coil.

the collector, the axial magnetic field (which is theoretically proportional to and in phase with the radial electric field for $f < f_{ci}$) undergoes a minimum rather than a maximum.

The data represented by plots such as those shown in Fig. IX-4 have been interpreted in two ways. In the first, we have plotted slopes of these curves against f. If we assume that a single wave is present, the results of this exercise should yield the real part (slope of phase curves) and the imaginary part (slope of log-amplitude curves) of the dispersion function. As shown in the sample plots of Fig. IX-4, there is, near the collector, some evidence of reflection. The reflected wave seems, however, to damp rapidly and thus there exist regions in which both the log-amplitude plots and phase plots are linear. It is in these

linear regions that the slopes were measured.

A second interpretation of the data is obtained by extrapolating the linear portions of the log-amplitude plots back to a point directly under the center of the coil. Under the assumption, again, that a single wave is present, the amplitude obtained should correspond to the amplitude of the coupling coefficient of the mode that is being measured, a quantity that has been calculated theoretically.

Results of these two interpretations are shown in Figs. IX-5 and IX-6 for two values of cathode current, and compared with theory developed in the author's thesis.[2] In obtaining the theoretical curves, two normalized effective collision frequencies (one accounting for ion collisions, the other for electron collisions) were adjusted to fit the data. Only the relative shape of the curves was taken into account. The ion collision frequency controls the width of the resonance curve, and its value was found to be in satisfactory agreement with an estimate of the ion-neutral collision frequency. The electron collision frequency controls the damping at the wave below resonance, and its value is approximately 8 times higher than an estimate based on electron-ion collisions. This result is similar to that obtained with the beam method of excitation of the waves (discussed in more detail in a previous report[1]). We are continuing our investigation of this effect.

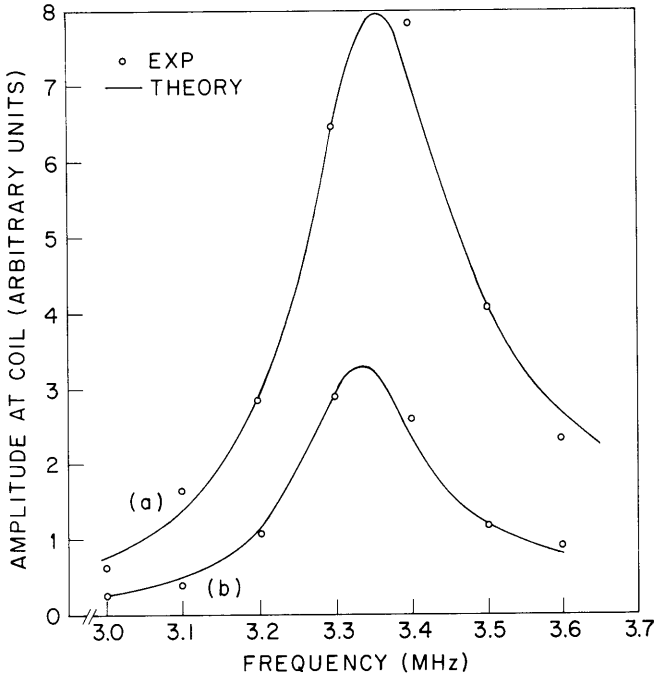

Fig. IX-5. Comparison of theoretical and experimental frequency dependence of amplitude under the coil. Curve (a): I_k = 5 amps, p = 1.15 μ. Curve (b): I_k = 10 amps, p = 1.15 μ.

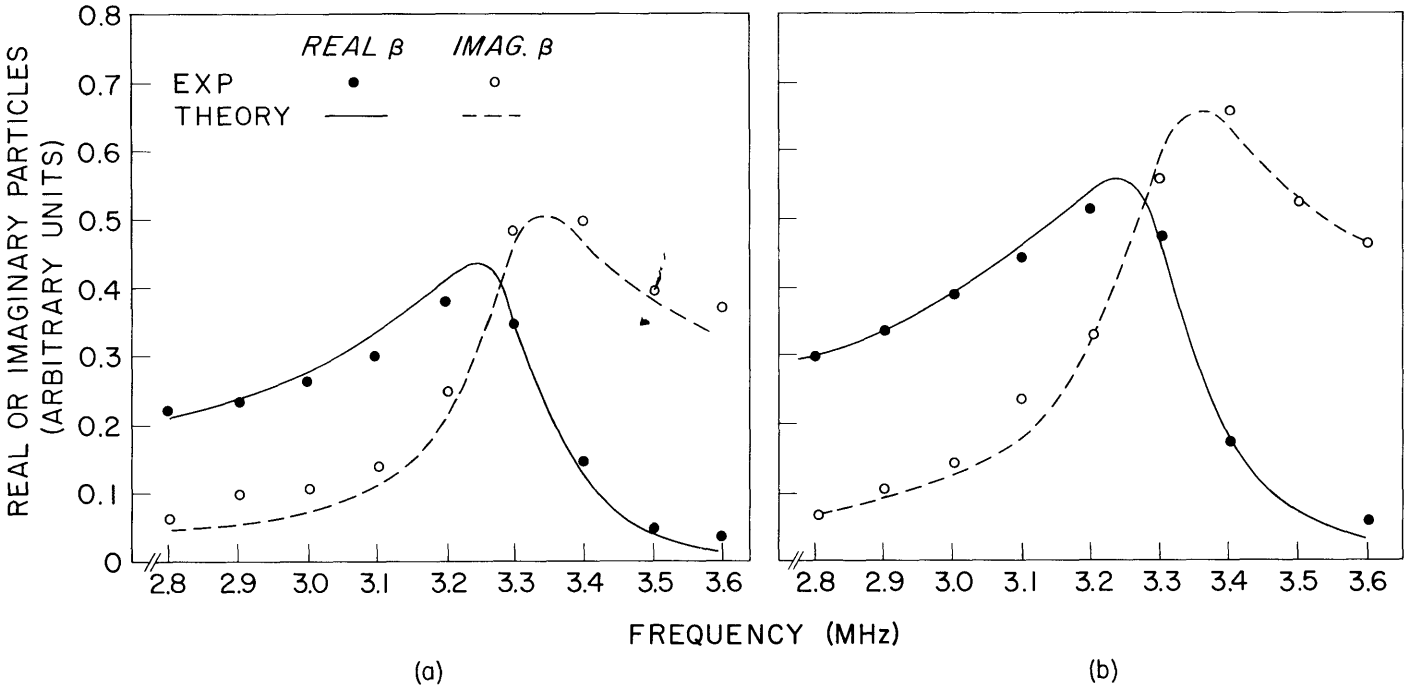

Fig. IX-6. Comparison of theoretical and experimental frequency dependence of the dispersion function. (a) I_k = 5 amps, p = 1.15 μ. (b) I_k = 10 amps, p = 1.15 μ.

Relation of These Results to the Heating Problem

Our purpose now is to relate these results to the problem of induction heating of a plasma. As will be made clear, knowledge of the response of the plasma to a current filament drive, a quantity that has been theoretically and experimentally determined, enables one to formulate and solve the problem of optimally coupling energy to the plasma ions. We shall consider below a specific method of heating, namely one in which the ion-cyclotron wave is launched in a region of magnetic field where the wave propagates ($\omega < \omega_{ci}$) and then propagates into a region of magnetic field where it is absorbed ($\omega = \omega_{ci}$). It is clear, however, that the formulation is sufficiently general to allow generalization to other heating schemes.

Consider the system shown in Fig. IX-7, which shows a coupling structure from which we desire to launch ion-cyclotron waves. Our experiments have shown that under typical plasma conditions, the coupling to the ion-cyclotron wave will be weak, and, in general, the average stored energy will be large compared with the energy radiated per cycle. Since the stored energy is associated with large fields that do not heat and are responsible for parasitic losses, that is, losses in the coil and vacuum walls, and breakdown, it is desirable to maximize the ratio of power radiated to energy stored.

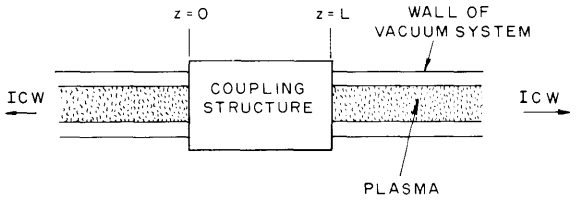

Fig. IX-7. Illustrating the problem of coupling ion-cyclotron waves (ICW) to a plasma column.

The coupling structure is assumed to be a coil whose turns are distributed over $0 < z < \ell$, according to a function n(z). We define a Green's function for this problem as the response of the azimuthal electric field at the coil radius caused by a single turn. We denote this function as $h(z - z')$, where z' is the position of the single turn.

Now, in general, the function h(z) may be decomposed by writing

$$h(z) = h_I(z) + h_{II}(z),$$

where $h_I(z)$ is the component attributable to the propagating ion-cyclotron wave, and $h_{II}(z)$ is the component associated with the cutoff wave that accounts for large (inductive) energy storage. With these definitions we may calculate the impedance of the coil as

$$\int_0^L dz'' \int_0^L dz'\, n(z')\, n(z'')\, h(z' - z''),$$

and the ratio of time-average power radiated, P, to time-average energy stored, W, is

$$\frac{P}{W} = 2\omega \frac{\int_0^L dz'' \int_0^L dz' \, n(z') \, n(z'') \, \mathrm{Re}\, h_I(z'-z'')}{\int_0^L dz'' \int_0^L dz' \, n(z') \, n(z'') \, \mathrm{Im}\, h_{II}(z'-z'')} \tag{1}$$

Application of variational techniques to Eq. 1 reveals that, for maximum P, n(z) obeys the equation

$$\int_0^L dz' \, n(z') \, \mathrm{Re}\, h_I(z'-z'') = \lambda \int_0^L dz' \, n(z') \, \mathrm{Im}\, h_{II}(z'-z''), \tag{2}$$

where λ is the maximum value of Eq. 1.

As an interesting application of this result we assume

$$\mathrm{Re}\, h_I(z-z') \sim \cos \beta_o (z-z')$$

$$\mathrm{Im}\, h_{II}(z-z') \sim \delta(z-z').$$

The meaning of the delta function here is that the wave number of the cutoff wave is much larger than β_o. Substitution in Eq. 2 leads to

$$\int_0^L dz' \, n(z') \cos \beta_o (z-z') = \lambda n(z).$$

This simple integral equation is easily solved. For simplicity, we assume $\beta_o L = m\pi$, in which case the solution is just

$$n(z) = A \cos (\beta_o z + \phi), \tag{3}$$

where A and ϕ are arbitrary constants. The solution in Eq. 3 represents the well-known periodic coupling coil first proposed by Stix.[3]

The discussion above has been concerned with a specific form of ion-cyclotron heating experiment, namely, one in which the RF is converted to ordered wave energy and thence to heat. It is also possible to conceive of an experiment in which the RF energy is absorbed directly from the coupling structure. The formulation above may be applied to this problem to maximize, for example, the ratio of energy absorbed by ions to stored energy or energy absorbed by electrons. In either event, ratios of the type in Eq. 1 are obtained, and the well-known techniques of optimum linear system theory may be applied to the problem. The experimental coil design would then be dictated by these considerations. Work continues on this problem.

R. R. Parker

References

1. J. A. Mangano and R. R. Parker, "System C: Excitation of an Ion-Cyclotron Resonance," Quarterly Progress Report No. 86, Research Laboratory of Electronics, M. I. T., July 15, 1967, pp. 147-154.

2. R. R. Parker, "Excitation and Propagation of Ion-Cyclotron Waves in a Plasma Column," Sc. D. Thesis, Department of Electrical Engineering, M. I. T., 1967.

3. T. H. Stix, Phys. Fluids 1, 308 (1958).

2. COMPUTER MODELS OF THE BEAM-PLASMA INTERACTION

Computer Models with a Uniform Plasma Density

We modeled the lossless one-dimensional beam-plasma interaction with a uniform plasma. The results are dramatically different from those obtained with a plasma density gradient along the direction of beam flow.[1,2] The model used is basically that of Dawson.[3] The plasma and beam electrons are represented by charge sheets, and the ions by an immobile neutralizing background. The beam is 1/99 as dense as the plasma. The beam is 2% velocity-modulated at $z = 0$ from $t = 0$ to $t = 150/\omega_p$, and unmodulated thereafter. Distances are normalized to the plasma intersheet spacing, $0.02\ v_o/\omega_p$, where v_o is the zero-order beam velocity. There are approximately 314 plasma sheets and 31.4 beam sheets per nominal wavelength ($2\pi\ v_o/\omega_p$). Energy is conserved within approximately 0.1% of the energy transferred from the beam to the plasma.

In Fig. IX-8 snapshots are shown of beam sheet velocity, the instantaneous acceleration (qE/m) of the sheets, plasma sheet velocity, and plasma density, all plotted against distance. The acceleration is normalized to $0.02\ v_o\omega_p$, the velocities to v_o, and the plasma density to its zero-order value. The snapshots are at times $1.5/\omega_p$ apart, starting at $t = 260/\omega_p$. We see that the beam has excited a traveling wave, which strongly affects both the beam and plasma. This wave is large only over a distance of approximately one wavelength. Over this distance the plasma sheets acquire peak oscillating velocities approaching $0.4\ v_o$, and peak plasma densities 5 times the zero-order plasma density. The beam is trapped by the wave near $z = 300$, and untrapped near $z = 500$. The wave has a phase velocity of $\approx 0.6\ v_o$. The beam is strongly scattered in velocity by the localized interaction.

The phenomena observed here are strikingly similar to those of the meniscus observed in a number of low-power beam-plasma experiments,[4-7] dating back to those of Langmuir.[8] The meniscus is a thin glowing region that contains strong plasma frequency oscillations and strongly scatters the beam electrons in velocity.

One criterion for the appearance of a meniscus in a beam-plasma interaction seems to be that the beam electrons have an injected kinetic energy corresponding to a potential not more than a few times the gas ionization potential. Then the peak plasma oscillatory kinetic energy will be below the ionization energy because trapping of plasma electrons by the wave will set an upper limit on the oscillation amplitude, if collisions or other losses do not. Hence the ionization will be primarily by the beam electrons, which

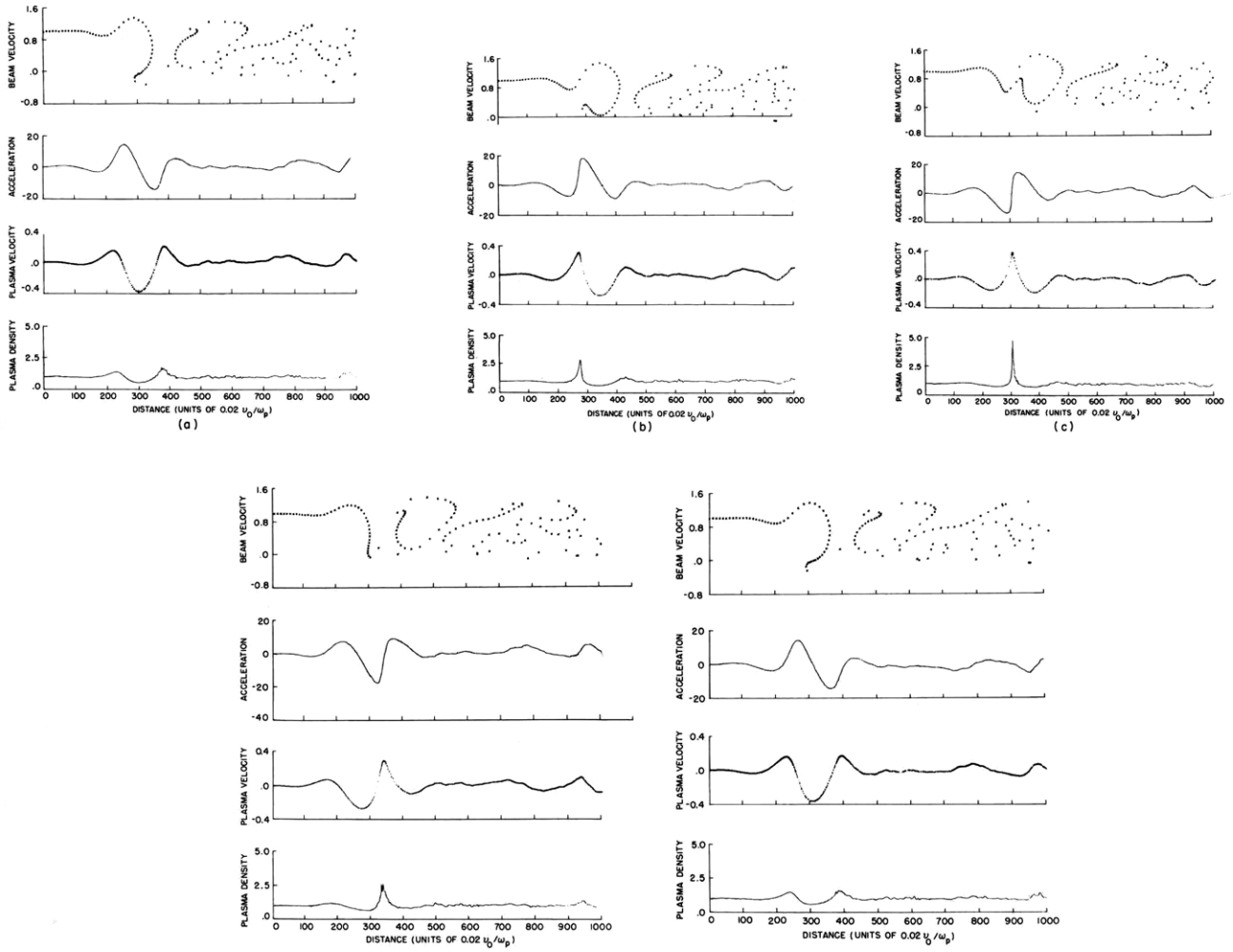

Fig. IX-8. (a) Beam-plasma interaction in a cold uniform plasma. $n_{po}/n_{bo} = 99$. Distance normalized to the plasma intersheet spacing, $0.02\ v_o/\omega_p$, acceleration to $0.02\ v_o\omega_p$, velocity to v_o, $t = 260/\omega_p$.

(b) $t = 261.5/\omega_p$.

(c) $t = 263/\omega_p$.

(d) $t = 264.5/\omega_p$.

(e) $t = 266/\omega_p$.

ionization should be axially uniform. If the main plasma loss is then radial, as it is in the long thin cylindrical tubes in which the meniscus is normally seen, the plasma density will be axially uniform.

The situation is quite different in experiments in which the beam potential is far above the ionization potential.[6,9] Secondary ionization by plasma electrons would be expected at the point where the meniscus would have formed. The resulting axial density gradients would then be expected to spread out the region of intense interaction. In our computer experiments with plasma density gradients along the direction of beam flow,[1,2] no meniscus is observed, nor is one seen in our laboratory experiments. In other workers' laboratory experiments at beam voltages of 100-400 volts,[6] only a diffuse, or spread-out meniscus is seen. At 700 volts[9] the interaction region is quite spread out, and strong plasma density gradients are measured.

In Fig. IX-9 we see a result of a computer experiment with the same conditions as in Figs. IX-8a-c, except that the beam density is 1/19 as dense as the plasma. In this

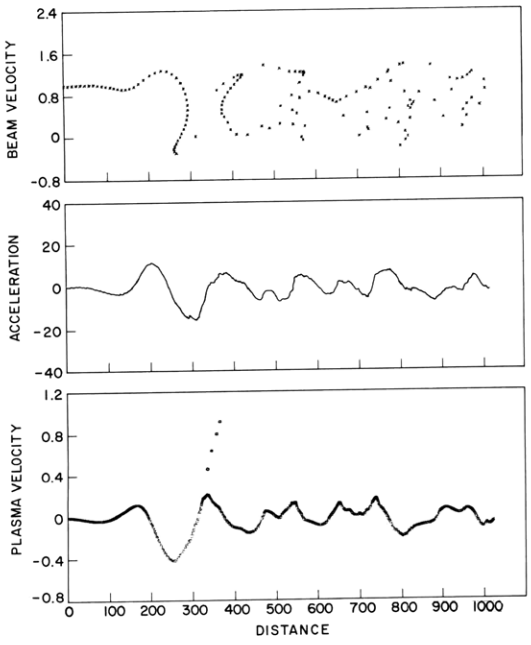

Fig. IX-9. Same conditions as Fig. IX-8, except that $n_{po}/n_{bo} = 19$, $t = 70/\omega_p$. The plasma sheets are held in by space charge at each end.

case, the interaction builds up much faster in time, so that by $t = 70/\omega_p$ trapping of the initially cold plasma electrons has occurred. We see no reason why this would not have occurred in the less dense beam case if we had let the programs run longer, which we did not do because of computer costs.

The interaction region is not localized as in the less dense beam case. This is possibly due to the speed with which the interaction grows. In the $n_{po}/n_{bo} = 99$ case the

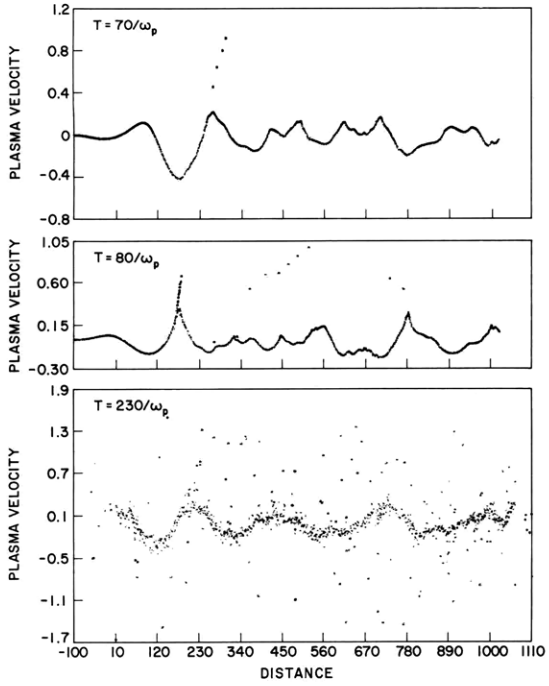

Fig. IX-10.

Snapshots of plasma sheet velocity at three different times, $n_{po}/n_{bo} = 19$.

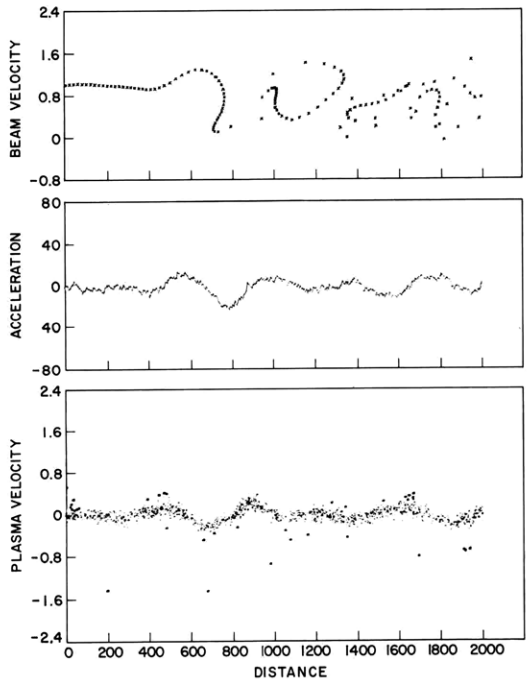

Fig. IX-11.

Beam-plasma interaction in a warm uniform plasma. The plasma sheets are initially assigned a Maxwellian temperature, such that $v_T = 0.075\ v_o$. 7.5 plasma sheets per Debye length, $t = 220/\omega_p$. Distance normalized to $0.01\ v_o/\omega_p$, acceleration to $0.01\ v_o\omega_p$.

meniscus first appears near the collector and works its way upstream. The beam deposits energy on the gun side of the meniscus, and extracts it from the collector side. In the $n_{po}/n_{bo} = 19$ case the strong interaction region moves upstream so quickly that perhaps it is not canceled efficiently downstream. Hence the initial transients persist. A comparison of plasma sheet velocities at 3 different times is shown in Fig. IX-10, $t = 230/\omega_p$; many of the plasma sheets have been trapped, and the rest of the plasma sheets have been thermalized.

In Fig. IX-11 we see the result of a case that includes plasma temperature. Here $n_{po}/n_{bo} = 99$, $v_T = .075\ v_o$, and the plasma is given a Maxwellian velocity distribution. Plasma sheets are reflected by hard walls at each end, whereas beam sheets are collected on the right, and fresh beam is injected on the left. We have 7.5 plasma sheets per Debye length. The principal result of including temperature is that trapping occurs at a lower field amplitude than in the cold case. Sheets in the tail of the velocity distribution and moving with the wave need be accelerated less than a cold sheet to reach the wave phase velocity. This trapping damps the wave and prevents it from growing larger.

Langmuir Probe Measurements

In the last quarter[2] we introduced a sinusoidal axial plasma density distribution into the computer model as a means of explaining the narrow collected beam velocity distribution observed experimentally in System A. We used a Langmuir probe to show that a density distribution approximating a sinusoid, in fact, exists.

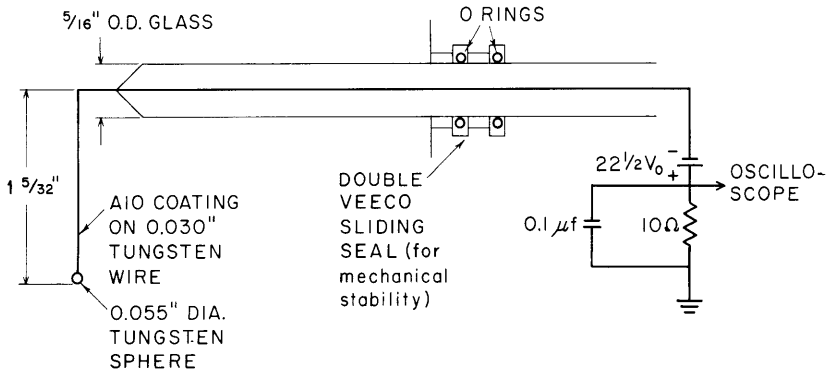

Fig. IX-12. Langmuir probe. The probe can slide axially and rotate radially into the plasma. Spherical tungsten tip, 0.055" in diameter.

A sketch of the Langmuir probe is shown in Fig. IX-12. The tip is a 0.055" diameter tungsten sphere. The probe axis is displaced radially 1 5/32" from the system axis. It can be moved axially, and the tip can be swung in an arc through the beam center.

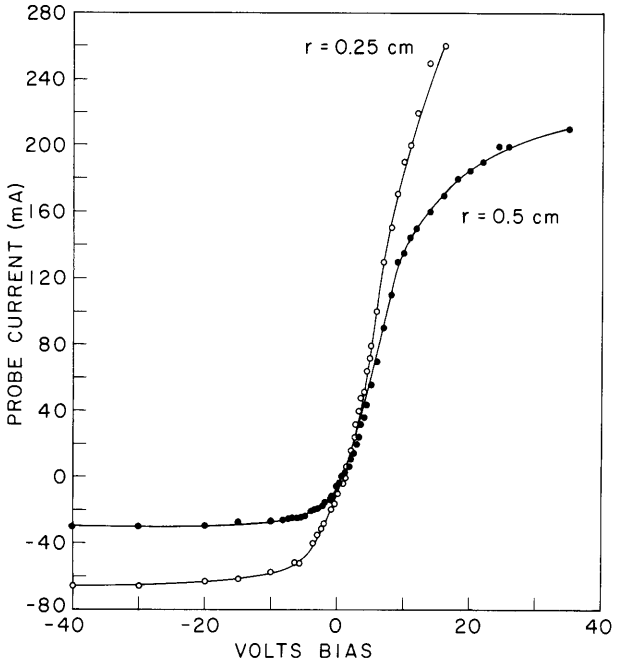

Fig. IX-13. Probe curves taken 20 cm from the anode. Beam voltage 8 kV, beam current 0.6 amp, H_2 pressure 1.4×10^{-3} Torr, magnetic field minimum of 430 Gauss, mirror ratio of 3. Data taken 300 μsec after beam turned on.

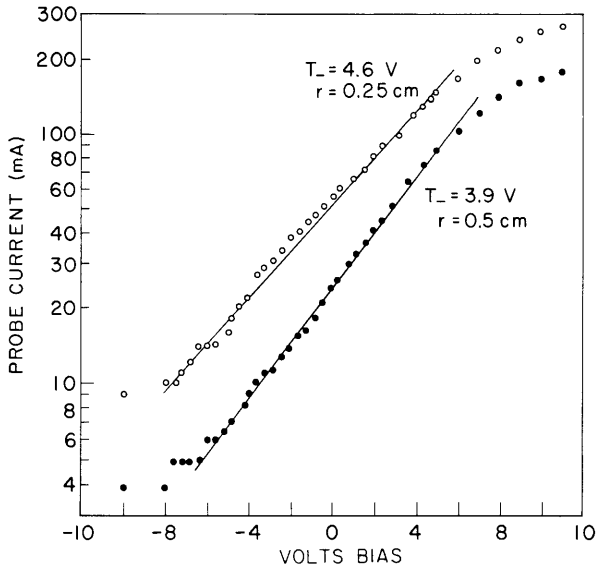

Fig. IX-14. Same as Fig. IX-13. The electron temperature is 4.6 volts at r = 0.25 cm, and 3.9 volts at r = 0.5 cm. The ion saturation current has been subtracted.

Hence measurements as a function of both axial and radial distance are possible.

Probe curves at two different radii at the midplane are shown in Fig. IX-13. The same data plotted on semi-log paper in Fig. IX-14 reveal an electron temperature of 4.6 volts at a distance of 0.25 cm from the beam axis, and of 3.9 volts at r = 0.5 cm.

The ion saturation current at the two fixed radii vs axial distance is shown in Fig. IX-15. These data are the average of symmetric points taken on each side of the beam. The probe tip would swing through the beam axis, as determined visually

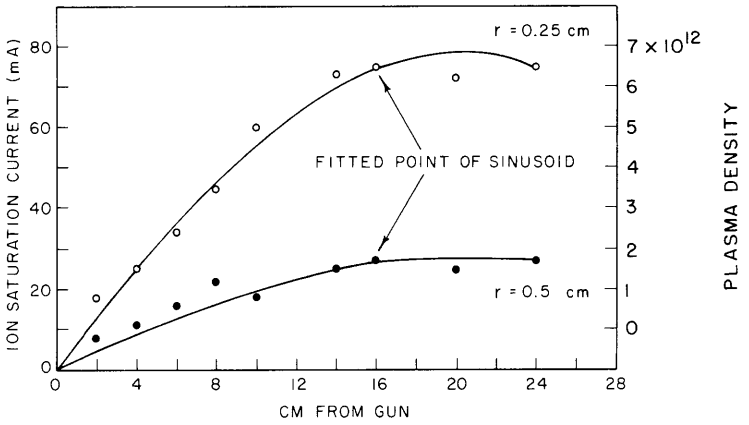

Fig. IX-15. Axial variation of ion saturation current at 2 fixed radii. Peak density is 7×10^{12}/cc. Probe biased at $0.22^{1/2}$ volt with respect to ground, and current read across 10Ω and 0.1 μf. in parallel. Beam current 0.5 amp, otherwise conditions same as Fig. IX-13.

through the glass drift tube, for the axial interval shown. It was not correctly aligned with the beam axis nearer the collector, so data there were not taken.

The density is related to the ion saturation current[11] by

$$I_+ = 0.4 q n_{po} A \left(\frac{qT_-}{M}\right)^{1/2}, \tag{1}$$

where I_+ is the ion saturation current, q the ion charge, n_{po} the plasma density, A the probe area, T_- the electron temperature, and M the ion mass. For our probe diameter of 0.055 in., a temperature of 4 volts, and ions of protons, Eq. 1 becomes

$$n_{po} = 9.19 \times 10^{13} I_+. \tag{2}$$

Our peak density at a radius of 0.25 cm is ~7×10^{12}/cc. This corresponds to a peak

plasma frequency of 24 GHz, in the upper range of the microwave radiation observed by Hsieh[12] in this system.

The ion saturation current as a function of radius at different axial positions is shown in Fig. IX-16. The data at the different axial positions lie along straight lines of roughly

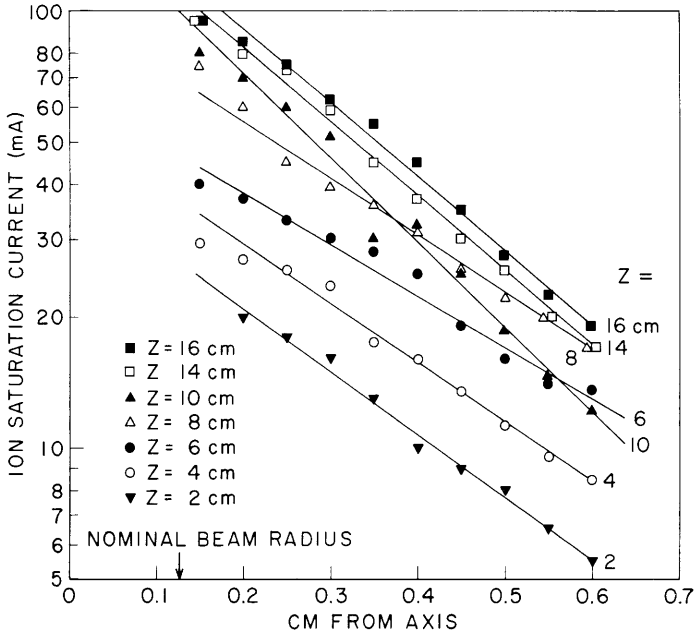

Fig. IX-16. Radial variation of ion saturation current, at different axial positions. At z = 16 cm the density decays as exp(-r/0.25), at z = 2 cm as exp(-r/0.30). The straight lines are a least means square fit, ignoring the points at r = 0.15 cm. The numbers beside each line indicate the axial distance from gun, in centimeters.

the same slope. At z = 16 cm the density decays as $e^{-r/.25}$, and at z = 2 cm as $e^{-r/.30}$. The nominal beam radius is 0.125 cm. The similarity of the slopes implies that the density at constant radii for different axial positions should be directly proportional to the density at the axis.

J. A. Davis

References

1. J. A. Davis, Quarterly Progress Report No. 84, Research Laboratory of Electronics, M. I. T., January 15, 1967, p. 145.

2. J. A. Davis, Quarterly Progress Report No. 86, Research Laboratory of Electronics, M. I. T., July 15, 1967, p. 156.

3. J. Dawson, Phys. Fluids 5, 445 (1962).

4. T. K. Allen, R. A. Bailey, and K. G. Emeleus, British J. Appl. Physics 6, 320 (1955).

5. F. W. Crawford and G. S. Kino, Proc. IRE 49, 1767 (1961).

6. F. W. Crawford and S. A. Self, J. Electronics 18, 569 (1965).

7. A. B. Cannara and F. W. Crawford, J. Appl. Phys. 36, 3132 (1965).

8. I. Langmuir, Phys. Rev. 26, 585 (1925).

9. S. M. Levitskii and I. P. Shashwin, Soviet Phys.-Tech. Phys. 11, 1018 (1966).

10. J. E. Hopson, J. Appl. Phys. 34, 2425 (1963).

11. D. Bohm, E. H. S. Burhop, and H. S. W. Massey, Characteristics of Electrical Discharges in Magnetic Fields, A. Guthrie and R. K. Wakerling (eds.) (McGraw-Hill Book Co., New York, 1949), Chap. 2.

12. H. Y. Hsieh, Ph. D. Thesis, Department of Electrical Engineering, M. I. T., September 1964.

3. THIN ELECTRON-BEAM INTERACTIONS WITH IONS IN A PLASMA-FILLED WAVEGUIDE

We shall report some results of a study on thin electron-beam interactions with ions in a plasma-filled waveguide.

The geometry of the beam-plasma system under consideration is shown in Fig. IX-17. The plasma uniformly fills the infinitely long cylindrical waveguide and consists of cold

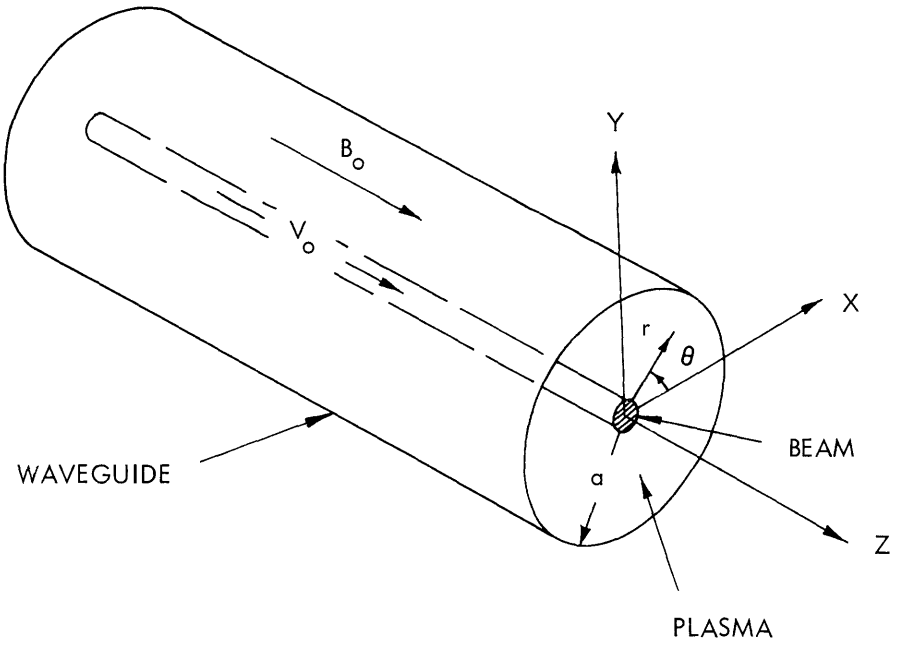

Fig. IX-17. Geometry of the beam-plasma system.

ions (density n_i), cold electrons (density n_c), and very hot electrons (density n_h) whose average thermal speed, v_{Te}, greatly exceeds the beam electron velocity v_o. The plasma is electrically neutral. A uniform, static axial magnetic field B_o is imposed on the system.

The electron beam travels with axial velocity v_o along the center of the waveguide. The beam has a circularly symmetric electron density profile given by $n_o(r)$, which is everywhere much smaller than the plasma density (n_i). The beam is thus considered to be fully neutralized by the plasma ions, and we neglect spatial inhomogeneities of plasma density. We restrict our attention to a thin electron beam confined within a radius small compared with the plasma-waveguide radius, a. A rigid-electron-beam model, proposed previously by Bers[1] is used. This model is appropriate if the transverse wavelength is large compared with the electron-beam diameter.

Dispersion Equations

The analysis follows a procedure outlined previously by Bers,[1] and has been carried out in detail in thesis research.[2] Waves of the form $\exp[j(\omega t - k_z z)]$ are assumed. A quasi-static approximation is made, and the electric potential in the plasma waveguide is represented as a sum of orthogonal modes:

$$\Phi = \mathrm{Re}\left[\sum_{m=-\infty}^{\infty}\sum_{n=1}^{\infty}\Phi_{mn}J_m(p_{mn}r)\,e^{-jm\theta}\,e^{j(\omega t-k_z z)}\right], \tag{1}$$

where p_{mn} is given by the n^{th} zero of $J_m(p_{mn}a)$. [Since m is an integer, $J_m(x) = (-1)^m J_{-m}(x)$ and $p_{mn} = p_{(-m)n}$.] It has been found that the rigid beam supports axisymmetric (m=0) space-charge modes, as well as transverse (m = ±1) synchronous and cyclotron modes. Modes with higher azimuthal variation are absent because the cross section of the rigid beam is assumed to suffer no distortion when the beam electrons displace transversely. The dispersion equations for the m = 0 and m = ±1 modes are

$$(\omega - k_z v_o)^2 = \sum_{n=1}^{\infty}\frac{\left(k_z^2/k^2\right)}{G(\omega, p_{on}, k_z)}\omega_{bon}^2; \quad (m=0) \tag{2a}$$

$$(\omega - k_z v_o)(\omega - k_z v_o \mp \omega_{ce}) = \sum_{n=1}^{\infty}\frac{\left(p_{ln}^2/k^2\right)}{G(\omega, p_{ln}, k_z)}\omega_{bln}^2; \quad (m=\pm 1). \tag{2b}$$

Here ω_{bon} and ω_{bln} are "effective beam-plasma frequencies" related to the beam density profile $n_o(r)$ and the potential distribution in the waveguide, as follows:

$$\omega_{bon}^2 = \frac{q_e^2 \langle n_o \rangle}{\epsilon_o m_e} \left[\frac{\int_0^a n_o(r)\, J_o(p_{on} r)\, r\, dr}{J_1(p_{on} a) \int_0^a n_o(r)\, r\, dr} \right]^2 \tag{3a}$$

$$\omega_{bln}^2 = \frac{q_e^2 \langle n_o \rangle}{\epsilon_o m_e} \left[\frac{\int_0^a \frac{\partial n_o(r)}{\partial r} J_1(p_{1n} r)\, r\, dr}{\sqrt{2} p_{1n} J_o(p_{1n} a) \int_0^a n_o(r)\, r\, dr} \right]^2, \tag{3b}$$

where

$$\langle n_o \rangle = \frac{1}{\pi a^2} \int_0^a \int_0^{2\pi} n_o(r)\, r\, dr d\theta.$$

In Eq. 2, $G(\omega, p_{mn}, k_z)$ is the quasi-static longitudinal dielectric constant for the (m,n) eigenmode in the plasma-filled waveguide, and is given by

$$G(\omega, p_{mn}, k_z) \cong \frac{p_{mn}^2}{k^2} K_{\perp c}(\omega) + \frac{k_z^2}{k^2} \left[K_{\| c}(\omega) + \frac{\omega_{ph}^2}{k_z^2 v_{Te}^2} \right], \tag{4}$$

where

$$k^2 = k_z^2 + p_{mn}^2$$

$$K_{\perp c}(\omega) = 1 - \frac{\omega_{pi}^2}{\omega^2 - \omega_{ci}^2} - \frac{\omega_{pc}^2}{\omega^2 - \omega_{ce}^2}$$

$$K_{\| c}(\omega) = 1 - \frac{\omega_{pi}^2}{\omega^2} - \frac{\omega_{pc}^2}{\omega^2}$$

$$\omega_{pi} = \sqrt{\frac{q_i^2 n_i}{\epsilon_o m_i}} = \text{ion plasma frequency}$$

$$\omega_{pc} = \sqrt{\frac{q_e^2 n_c}{\epsilon_o m_e}} = \text{cold-electron plasma frequency}$$

$$\omega_{ph} = \sqrt{\frac{q_e^2 n_h}{\epsilon_o m_e}} = \text{hot-electron plasma frequency}$$

$v_{Te} = \sqrt{\frac{\kappa T_e}{m_e}}$ = thermal speed of hot (Maxwellian) electrons

m_e, m_i = electron, ion masses

q_e, q_i = electron, ion charges

ω_{ce}, ω_{ci} = electron, ion cyclotron frequencies.

In Eq. 4 we have made the assumptions $(\omega/k_z v_{Te}) \ll 1$ and $\left(p_{mn}^2 v_{Te}^2/\omega_{ce}^2\right) \ll 1$. For beam-plasma interactions, the first assumption implies $v_{Te} \gg v_o$, and allows us to neglect Landau damping by the electrons. The second assumption imposes an upper bound on the value of p_{mn} which can be considered without taking into account the effects of finite Larmor radius. A more general expression for the quasi-static longitudinal dielectric constant may be found elsewhere.[1,2]

We consider the case in which ions are singly charged. The charge neutrality condition then demands

$$n_i = n_c + n_h,$$

or equivalently,

$$\omega_{pi}^2\left(\frac{m_i}{m_e}\right) = \omega_{pi}^2\left(\frac{\omega_{ce}}{\omega_{ci}}\right) = \omega_{pc}^2 + \omega_{ph}^2.$$

Note that the dispersion equation for the (m, n) eigenmode in a plasma-filled waveguide (with no beam) is given by setting the longitudinal dielectric constant $G(\omega, p_{mn}, k_z)$ to zero. The infinite sums appearing on the right sides of Eq. 2 signify that the beam interacts with all of the eigenmodes in the plasma waveguide. In the vicinity of the regions where the beam waves are synchronous with the n^{th} plasma eigenmode, however, $G(\omega, p_{mn}, k_z)$ tends to zero. We then assume that the n^{th} term in each infinite sum of Eq. 2 dominates. The dispersion equations then take the approximate forms

$$(\omega - k_z v_o)^2 \left[p_{on}^2 K_{\perp c}(\omega) + k_z^2\left(K_{\parallel c}(\omega) + \frac{\omega_{ph}^2}{k_z^2 v_{Te}^2}\right)\right] = k_z^2 \omega_{bon}^2; \quad (m = 0) \tag{5a}$$

$$(\omega - k_z v_o)(\omega - k_z v_o \mp \omega_{ce})\left[p_{ln}^2 K_{\perp c}(\omega) + k_z^2\left(K_{\parallel c}(\omega) + \frac{\omega_{ph}^2}{k_z^2 v_{Te}^2}\right)\right] = p_{ln}^2 \omega_{bln}^2; \quad (m = \pm 1) \tag{5b}$$

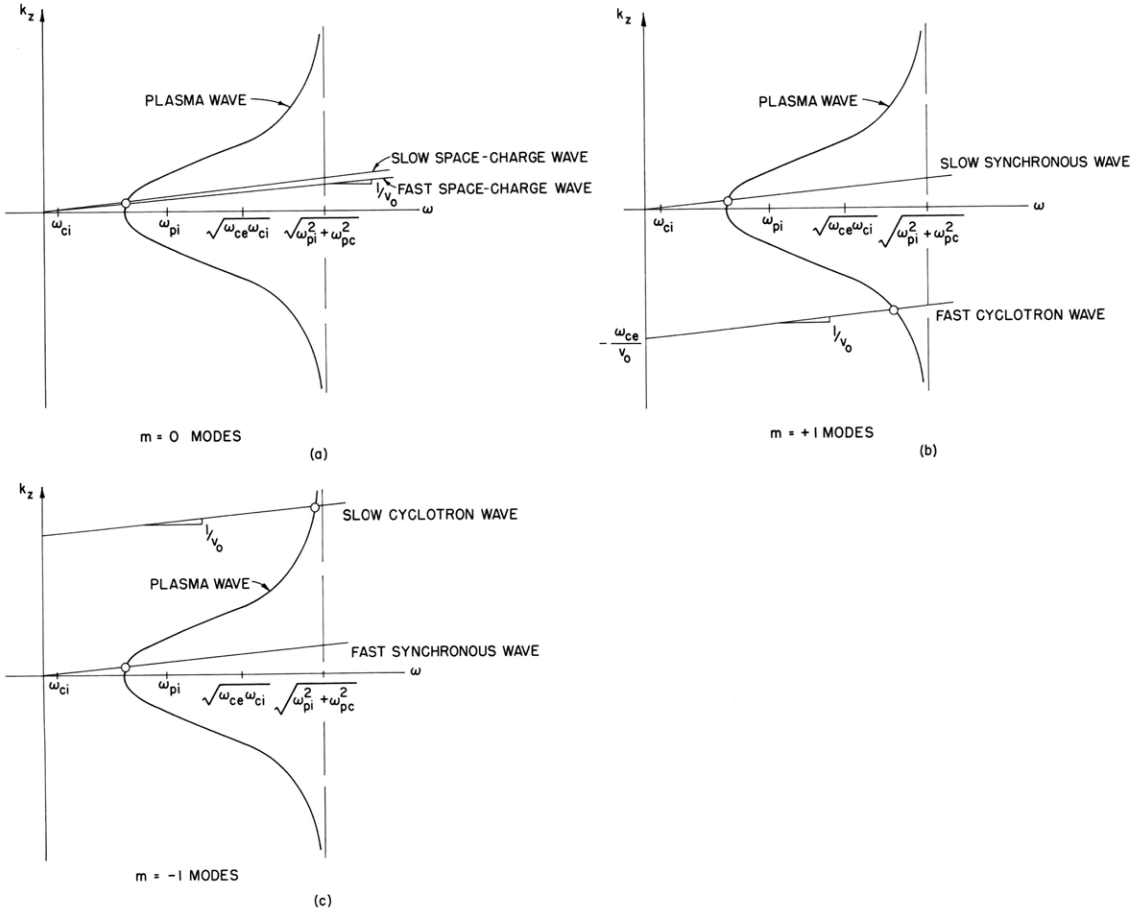

Fig. IX-18. Synchronous interactions of a thin electron beam in a plasma-filled waveguide. Regions of synchronism are indicated by circles. The m = +1 and m = -1 modes are right and left circularly polarized, respectively.

Figure IX-18 shows the regions where synchronism occurs between the beam waves and a typical plasma eigenmode. We confine our attention to the low-frequency range defined by $\omega_{ci} < \omega < \sqrt{\omega_{ce}\omega_{ci}}$, in which ion interactions can occur.[3]

Synchronous Amplification Rates for a Weak Beam

For a weak beam, Eq. 5 gives the following amplification rates for the slow beam waves at synchronism with the n^{th} plasma eigenmode:

$$k_{zi} = \frac{\sqrt{3}}{2}\left|\left(\frac{\omega_{bon}}{v_o}\right)^2 \left(\frac{\omega}{v_o}\right)\frac{1}{2K_{\|c}(\omega)}\right|^{1/3} \qquad \text{(m = 0 slow space-charge wave)} \qquad (6a)$$

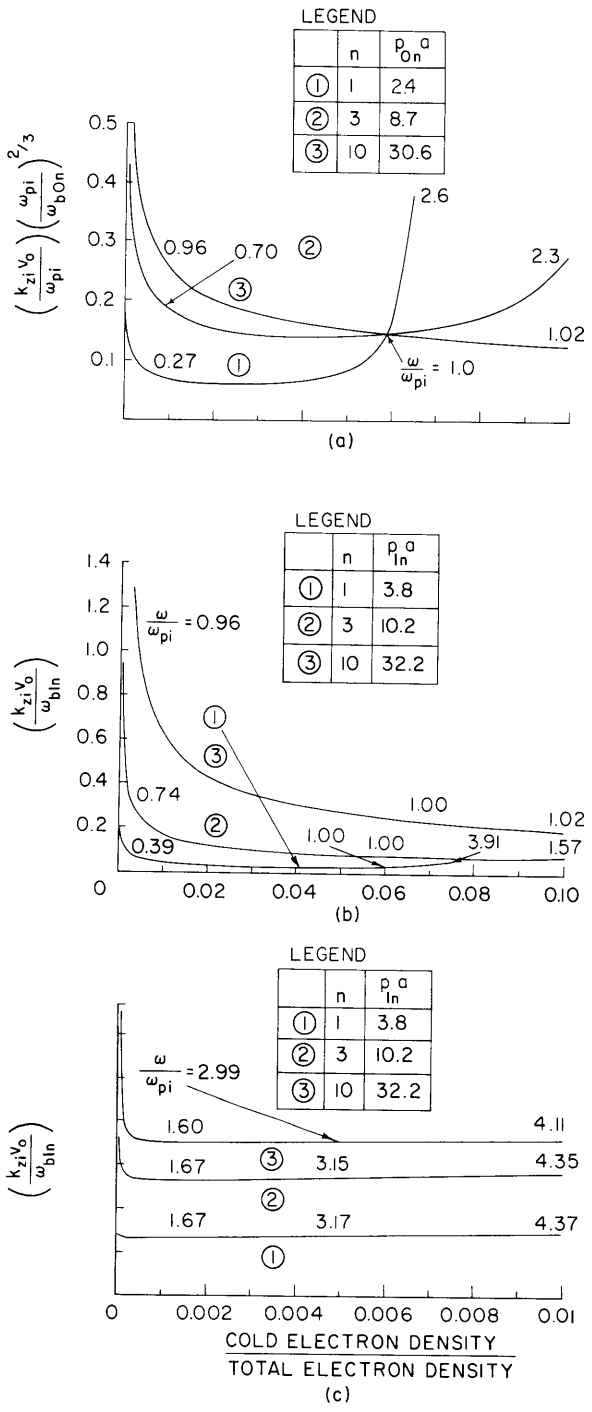

Fig. IX-19. Synchronous amplification rates vs relative cold electron concentration in plasma.
(a) Slow space-charge wave amplification.
(b) Slow synchronous wave amplification.
(c) Slow cyclotron wave amplification.
Numbers along curves indicate the normalized synchronous frequencies (ω/ω_{pi}). Parameters used are: $\omega_{pi} = 20\ \omega_{ci}$; $\omega_{ce} = 1836\ \omega_{ci}$; $v_{Te} = 4\ v_o$; $(a\omega_{pi}/v_o) = 0.9$.

$$k_{zi} = p_{ln} \frac{\omega_{bln}}{\sqrt{\omega\,\omega_{ce}}} \left| \frac{1}{2K_{\|c}(\omega)} \right|^{1/2} \qquad (m = +1 \text{ slow synchronous wave}) \tag{6b}$$

$$k_{zi} = p_{ln} \frac{\omega_{bln}}{\omega_{ce}} \left| \frac{1}{2K_{\|c}(\omega)} \right|^{1/2} \qquad (m = -1 \text{ slow cyclotron wave}). \tag{6c}$$

Expressions (6) are to be evaluated at the synchronous frequencies.

Figure IX-19 shows the calculated amplification rates for the slow beam waves at synchronism with three different plasma modes, as a function of the relative cold electron concentration in the plasma. These calculations were done for fixed ω_{pi}/ω_{ci}, $a\omega_{pi}/v_o$, and v_{Te}/v_o, as shown. The normalized synchronous frequencies are indicated along each curve. As the relative cold electron concentration is increased, the synchronous frequencies are seen to shift upward. This shift is more pronounced for the cyclotron waves than for the space-charge or synchronous waves.

In Fig. IX-20 we show the amplification rates as a function of frequency for the slow space-charge and synchronous waves, when no cold electrons are present in the

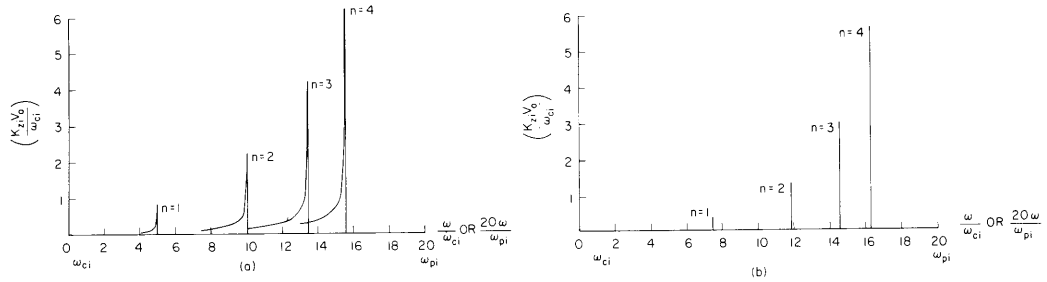

Fig. IX-20. Amplification vs frequency in a hot-electron plasma waveguide.
(a) Slow space-charge wave amplification vs frequency.
(b) Slow synchronous wave amplification vs frequency.
A thin electron beam of radius b = 0.01 a and uniform density $n_b = 0.0136\, n_i$ is assumed. All the plasma electrons are hot. Other parameters are: $\omega_{pi} = 20\, \omega_{ci}$; $\omega_a = 1836\, \omega_{ci}$; $v_{Te} = 4\, v_o$; $(a\omega_{pi}/v_o) = 0.9$.

plasma. A thin uniform electron beam of radius b = 0.01 a and a density $n_b = 0.0136\, n_i$ was assumed. These amplification rates were obtained by superimposing the numerical solutions of Eq. 5 for the lowest 4 plasma eigenmodes. The amplification for the slow synchronous wave (Fig. IX-20b) is confined to very narrow bands at synchronism with the plasma modes. In contrast, the amplification for the slow space-charge wave (Fig. IX-20a) occurs over a much broader range of frequencies, although pronounced

peaks are still observed at synchronism. The broadband nature of space-charge wave amplification is due to reactive medium interactions involving the slow and fast space-charge waves when the longitudinal dielectric constant of the plasma is negative. A corresponding reactive medium amplification does not seem to exist for the transverse waves, at least with the parameters used. This is probably because of the great disparity between the phase velocities of the synchronous and cyclotron waves of like polarization. The amplification for the slow cyclotron wave is also confined to very narrow bands at synchronism near plasma resonance (this is not shown).

Figure IX-21 shows how the amplification rates versus frequency are changed when 5% of the plasma electrons are cold and the rest are hot. Comparing Fig. IX-21 with the corresponding parts of Fig. IX-20, we note that (i) the peaks have shifted upward in frequency, corresponding to increases in the synchronous frequencies; (ii) the amplification is considerably more broadband than when cold electrons are absent. For the space-charge wave there is considerable overlap between the amplification curves calculated from Eq. 6 for the 4 lowest plasma modes. This overlap is much less significant for the slow synchronous wave, again, because of the absence of reactive medium amplification; and (iii) the amplification rates in Fig. IX-21 are much smaller than those for Fig. IX-20. This is consistent with Fig. IX-19.

An interesting phenomenon occurs as the relative cold-electron concentration in the plasma is increased from zero (with other parameters, including the total electron density, held fixed). We have noted that this is accompanied by an upward shift in the synchronous interaction frequencies. This shift is more rapid, however, for interactions involving the lower order plasma modes, as can be observed from Figs. IX-20 and 21. Thus, as the relative cold-electron concentration is increased, the peaks of amplification versus frequency come closer together. At some value of relative cold-electron concentration, all of the peaks coincide at the same frequency. This is the situation when the beam wave is synchronized to all of the plasma modes at the same frequency. For the space-charge and synchronous waves, Fig. IX-19 shows this to happen when roughly 5.9% of the plasma electrons are cold. In this special case the amplification rate is calculated from Eq. 5 to be

$$k_{zi} = \frac{\sqrt{3}}{2}\left|\sum_{n=1}^{\infty}\left(\frac{\omega_{bon}}{v_o}\right)^2\left(\frac{\omega}{v_o}\right)\frac{1}{2K_{\|c}(\omega)}\right|^{1/3} \qquad \text{(m = 0 slow space-charge wave)} \tag{7a}$$

$$k_{zi} = \left|\sum_{n=1}^{\infty} p_{ln}^2\,\omega_{bln}^2\left(\frac{1}{\omega\,\omega_{ce}}\right)\frac{1}{2K_{\|c}(\omega)}\right|^{1/2} \qquad \text{(m = +1 slow synchronous wave)} \tag{7b}$$

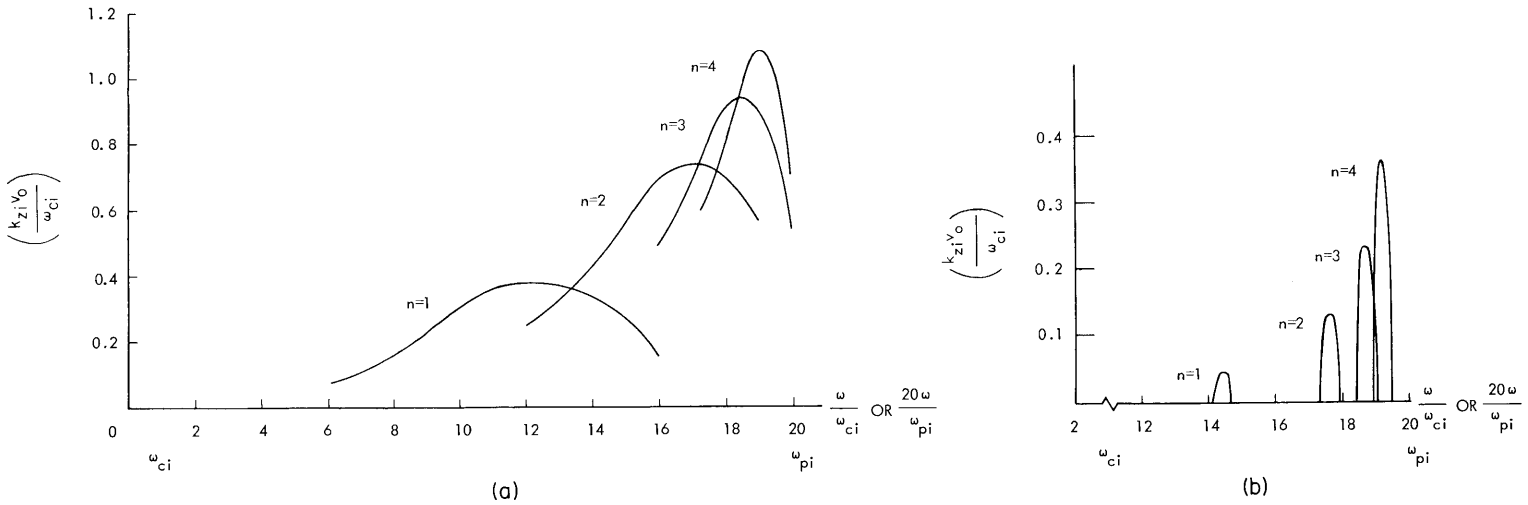

Fig. IX-21. Amplification vs frequency in a plasma waveguide with 5% cold electrons and 95% hot electrons.
(a) Slow space-charge wave amplification vs frequency.
(b) Slow synchronous wave amplification vs frequency.
Parameters are the same as in Fig. IX-20, except that 5% of the plasma electrons are cold. The total electron density is unchanged.

These expressions differ from those in Eq. 6, in that a sum over all n is involved. In deriving (6) it was assumed that the beam waves interacted with each plasma eigenmode separately (that is, the beam waves synchronized to different plasma modes at different frequencies). The amplification rates given by (7) are much larger than those predicted by (6), but their physical significance cannot be ascertained until the effects of finite Larmor radius on interactions involving very high order plasma modes are studied.

Absolute Instabilities

The case of a homogeneous beam filling the waveguide, with a plasma containing only hot electrons ($\omega_{pc} = 0$) was first considered by Briggs.[4] For the model of the present work (thin inhomogeneous beam in a plasma waveguide with both hot and cold plasma electrons), low-frequency absolute instabilities were found to occur at reasonable beam densities for either space-charge or synchronous wave interaction with a single plasma mode. The conditions for the instability were derived from Eq. 5, and are the following:

$$\omega_{bon}^2 > \omega_{pi}^2 + \omega_{pc}^2 - \omega_{ci}^2 - \frac{p_{on}^2 \omega_{pi}^2}{p_{on}^2\left(1 + \omega_{pc}^2/\omega_{ce}^2\right) + (\omega_{ph}/v_{Te})^2 + (\omega_{bon}/v_o)^2}$$

(m = 0 slow space-charge wave) (9a)

$$p_{ln}\omega_{bln}^2\left(\frac{p_{ln}v_o}{\omega_{ce}}\right) > \frac{8}{9}k_z\left(\omega_{pi}^2 + \omega_{pc}^2 - \omega^2\right) \quad \text{(m = +1 slow synchronous wave).} \qquad (9b)$$

In Eq. 9b, k_z and ω are the axial wave number and frequency at the onset of the absolute instability; both are pure real and given by

$$k_z = \frac{\omega}{3v_o}$$

$$3k_z^2 K_{\|c}(\omega) - p_{ln}^2 K_{\perp c}(\omega) - \left(\frac{\omega_{ph}}{v_{Te}}\right)^2 = 0.$$

The absolute instabilities for the slow space-charge and slow synchronous waves occur at frequencies near or below the ion plasma frequency ω_{pi} (possible absolute instabilities in the high-frequency range were not studied).

When $\omega_{pc} \gg \omega_{pi}$, the condition for absolute instability of the slow space-charge wave is very nearly given by

$$\omega_{bon}^2 > \omega_{pc}^2,$$

which shows that even small concentrations of cold electrons in the plasma tend to

"short out" the instability.

The condition for absolute instability of the slow synchronous wave is less restrictive when cold electrons are present, as shown in Fig. IX-22. For large transverse wave numbers p_{ln}, even rather low beam densities can cause an absolute instability. The

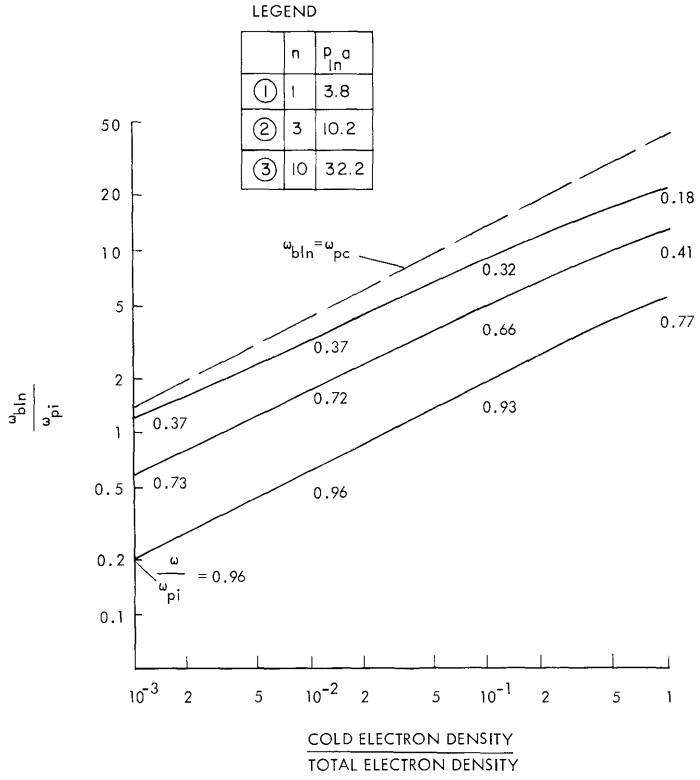

Fig. IX-22. Onset conditions for absolute instability of synchronous wave interaction as a function of relative cold electron concentration. An absolute instability exists if ω_{bin} exceeds the value given by each curve. Normalized frequencies (ω/ω_{pi}) at the onset of the instability are indicated along the curves. Parameters used: $\omega_{pi} = 20\ \omega_{ci}$; $\omega_a = 1836\ \omega_{ci}$; $v_{Te} = 4\ v_o$; $(a\omega_{pi}/v_o) = 0.9$.

effects of finite Larmor radius should be taken into account, however, when the transverse wavelength becomes comparable to the Larmor radius of the hot electrons.

It should also be emphasized that the conditions in Eq. 9 were derived by considering only beam interactions with a single plasma mode. We intend to study the consequences of beam interaction with several plasma modes simultaneously, and to further investigate the physical relevance of the instabilities discussed in this report.

S. Chou, A. Bers

References

1. A. Bers, "Theory of Beam-Plasma Interactions," Quarterly Progress Report No. 85, Research Laboratory of Electronics, M. I. T., April 15, 1967, p. 163.
2. S. Chou, "Electron Beam Interactions with Ions in a Plasma," S. M. Thesis, Department of Electrical Engineering, M. I. T., Cambridge, Mass., September 1967.
3. M. A. Lieberman and A. Bers, "Theory of VHF Oscillations and Possible Interactions with Ions in the Beam-Plasma Discharge," Quarterly Progress Report No. 81, Research Laboratory of Electronics, M. I. T., April 15, 1966, p. 85.
4. R. J. Briggs, Electron-Stream Interaction with Plasmas (The M. I. T. Press, Cambridge, Mass., 1964).

4. ALTERNATIVE STABILITY ANALYSES

The usual formulation of the pole-pinch method[1,2] for distinguishing convective and absolute instabilities requires a solution of the dispersion equation, $D(\omega, k) = 0$, for k as a function of ω. In many cases of interest, such as problems involving warm plasmas in a magnetic field, the dispersion equation may be more easily solvable for $\omega(k)$ rather than $k(\omega)$. In an alternative formulation of the stability problem,[3] attention is focused on the function $\omega(k)$, and we are now investigating the rigorous foundation and relative generality of these other approaches in the hope that alternative procedures for stability analysis might result.

We start from the usual expression for the impulse response of an infinite system:

$$\phi(z,t) = \int_F \int_L \frac{N(\omega,k)}{D(\omega,k)} e^{j(\omega t - kZ)} \frac{d\omega dk}{(2\pi)^2}. \tag{1}$$

In Eq. 1, $\phi(z,t)$ is the impulse response, $N(\omega,k)$ is considered to be an entire function of ω and k, the integration over frequency ω is along a Laplace contour, L, in the lower half ω-plane, and the integration over k is along the Fourier contour F (the real-k axis).

The pole-pinch method of determining the asymptotic behavior of $\phi(z,t)$ follows by performing the integration over k before the ω-integration is performed. If we instead perform the ω-integration first, we obtained from residue calculus

$$\phi(z,t) = j \int_{-\infty}^{\infty} \sum_{\kappa} \frac{N(\omega_\kappa k)}{\left.\frac{\partial D}{\partial \omega}\right|_{\omega_\kappa(k)}} e^{j[\omega_\kappa(k)t - kz]} \frac{dk}{2\pi}, \tag{2}$$

where the $\omega_\kappa(k)$ are all of the solutions for ω of $D(\omega,k) = 0$, that is, the normal modes of the system. If the response is to grow in time, there must be at least one unstable mode that is a solution to the dispersion equation, say $\omega_\kappa(k)$, for which Eq. 3 is satisfied.

$$\text{Im } \omega_\kappa(k) < 0 \qquad a < k < b, \tag{3}$$

where a and b are real numbers. See Fig. IX-23.

At points where the normal modes are degenerate (the branch points of $\omega_\kappa(k)$), $\partial D/\partial\omega = 0$, and individual terms in the sum in Eq. 2 are singular. It can be shown that the sum is an entire function of k; the singularities in individual terms cancel.

If we assume that the lower half ω-plane is free from branch points of $\omega_\kappa(k)$, then we obtain the criteria of Fainberg, Kurilko, and Shapiro as follows. Focusing attention on one term in the sum in Eq. 2, we find that the asymptotic behavior of $\phi(z,t)$ is determined by the asymptotic limit of

$$I(t,z) = \int_F e^{j(\omega_\kappa(k)t-kz)}\, dk \tag{4}$$

which, with a change of variables, can be written

$$I(z,t) = \int_C \frac{e^{j(\omega_\kappa t-k(\omega)z)}}{(d\omega_\kappa(k)/dk)}\, d\omega_\kappa. \tag{5}$$

The contour C is the conformal mapping of the real-k axis into the ω-plane. If a saddle point of $\omega_\kappa(k)$ exists between the C contour and the real ω-axis (the shaded region of Fig. IX-23) the response increases exponentially with time (absolute instability); otherwise the instability is convective.[3]

It has been shown that difficulties in the criteria arise when there are branch points of $\omega_\kappa(k)$ in the shaded region of Fig. IX-23.[4] In this report we would like to demonstrate a physical example in which there could be difficulty in interpretation even when there are no branch points of $\omega_\kappa(k)$ in the lower half-plane.

The example is a one-dimensional monoenergetic beam moving with velocity v_o through a resistive background moving with velocity -v. The electrostatic waves obey the dispersion relation.

$$(\omega-kv_o)^2 = \frac{\omega_p^2}{1 + \dfrac{\sigma/\epsilon_o}{j(\omega+kv)}}, \tag{6}$$

where ω_p is the plasma frequency of the beam, σ is the conductivity of the background and ϵ_o is the free-space permittivity. This dispersion equation has been investigated for two different sets of parameter values.

For $\frac{v}{v_o} = 0.25$, $\frac{\omega_p \epsilon_o}{\sigma} = 1$, we see from Fig. IX-24a that there is a branch point

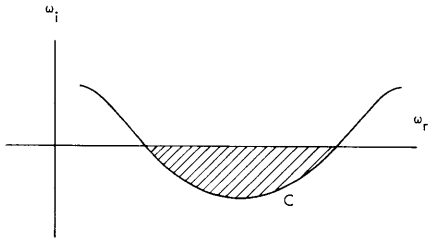

Fig. IX-23. The C contour is a map of the real-k axis into the ω-plane under the transformation $\omega = \omega_\kappa(k_r)$. The shaded region is intended to indicate that portion of the ω-plane which is in the lower half-plane between the C contour and the real-ω axis.

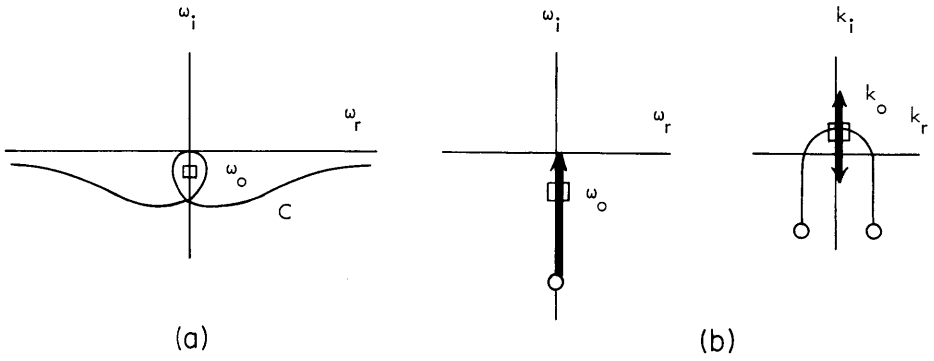

Fig. IX-24. Analysis of Eq. 7 for $\frac{v}{v_o} = 0.25$, $\frac{\omega_p \epsilon_o}{\sigma} = 1$. (a) Complex ω for real k. There is a branch point of $k(\omega)$ at $\omega = \omega_o$. (b) Locus of roots in k-plane for application of the pole-pinch analysis.

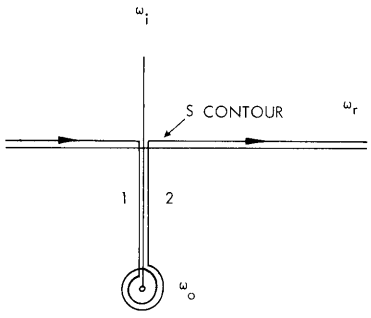

Fig. IX-25. The S contour.

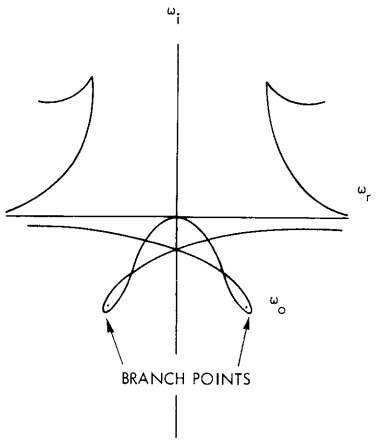

Fig. IX-26. Locus of $\omega(k_r)$ for $\frac{v}{v_o} = 4$, $\frac{\omega_p \epsilon_o}{\sigma} = 1$.

of $k(\omega)$ (saddle point of $\omega(k)$) in the lower half ω-plane between the C contour and the real-ω axis; however, according to the pole-pinch method illustrated in Fig. IX-24b, the instability is convective. We reason our way out of the dilemma as follows.

Consider Eq. 5 and deform the C contour of Fig. IX-24a into the S contour illustrated in Fig. IX-25. In the vicinity of $\omega = \omega_o$,

$$(\omega-\omega_o) \sim (k-k_o)^2 \tag{7}$$

and therefore

$$\frac{d\omega}{dk} \sim (\omega-\omega_o)^{1/2}. \tag{8}$$

Since the S contour rotates <u>twice</u> (a total of 4π radians) around the branch pole of the integrand of Eq. 5, the contribution along contours (1) and (2) in Fig. IX-25 cancels, and $I(t) \to 0$ as $t \to \infty$.

For $\frac{v}{v_o} = 4$, $\frac{\omega_p \epsilon_o}{\sigma} = 1$, the $\omega(k_r)$ contours are sketched in Fig. IX-26. Observe that the C contour wraps only once about the branch points, and therefore the evaluation of Eq. 5 yields

$$\phi(z,t) \sim \frac{e^{j\omega_o t}}{\sqrt{t}}, \qquad t \to \infty, \tag{9}$$

in agreement with the pole-pinch analysis.

It is also of some interest to consider the asymptotic evaluation of Eq. 2 using the well-known saddle-point approach[5]; particularly since the integrand in Eq. 2 is an entire function. The modulus of the integrand is presented in Fig. IX-27 for the two cases previously discussed. For the case of no absolute instability, see Fig. IX-27a. If we require the steepest descents path (SDC) to pass through the saddle point k_o and to end at ($k_r = \infty$, k_i = finite number) and also that the modulus be smaller than its value at k_o for all values of k along the SDC, we would require that the SDC double back on itself at k_o, because of the topology of Fig. IX-25a.

On the other hand, for the case illustrated in Fig. IX-27b, we see that a saddle-point evaluation would give a nonzero result, since it is possible topologically to extend the SDC contour through the saddle point without doubling back on itself.

In conclusion, we have demonstrated the following stability criterion, which is valid when (i) there is only one unstable mode, (ii) the shaded region of the lower half ω-plane in Fig. IX-23 is free from branch points of $\omega(k)$, and (iii) the unstable points of $\omega(k)$ in the lower half-plane satisfy Eq. 7, which is the most frequent type of singularity encountered in practice.

The system exhibits absolute instability when deformation of the C contour

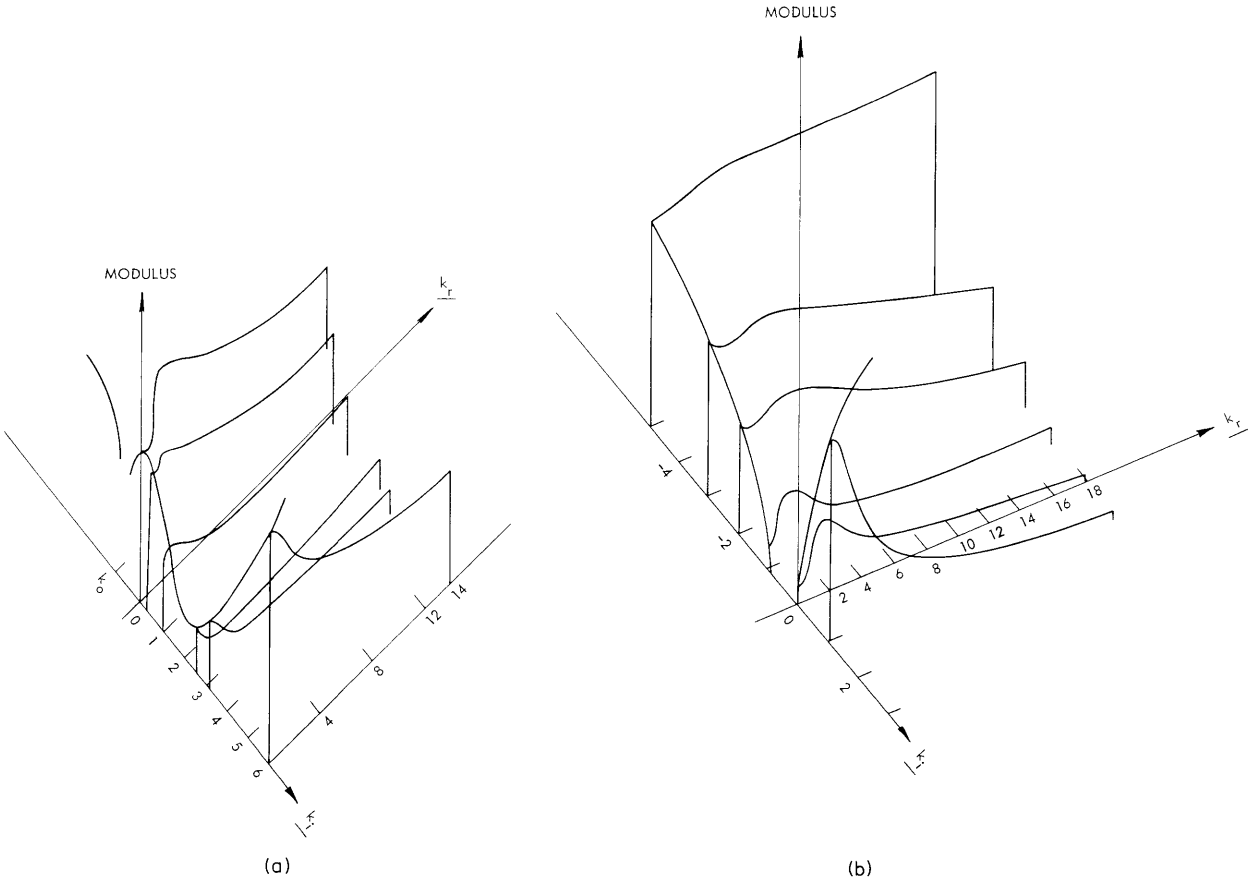

Fig. IX-27. Modulus of the integrand in Eq. 2 plotted as a function of k, with the dispersion equation (6) used. The modulus is symmetric with respect to the imaginary k-axis. $\underline{k} = \frac{kv_o\epsilon_o}{\sigma}$. (a) $\frac{v}{v_o} = 0.25$, $\frac{\omega_p\epsilon_o}{\sigma} = 1$, t = 10. The saddle point of interest is at $\underline{k}_o = 0.15$ j. (b) $\frac{v}{v_o} = 4$, $\frac{\omega_p\epsilon_o}{\sigma} = 1$, t = 10. The saddle point is at $\underline{k}_o = 1.7 - 0.05$ j. The scale is logarithmic.

(see Fig. IX-23) of the kind illustrated in Fig. IX-25 leads to an S contour that wraps once or an odd number of times about a branch point in the lower half ω-plane. If the deformation wraps around such a branch point an even number of times, the instability is convective.

We are now investigating generalizations of this method.

G. W. Goddard, R. J. Briggs

References

1. A. Bers and R. J. Briggs, "Criteria for Determining Absolute Instabilities and Distinguishing between Amplifying and Evanescent Waves," Quarterly Progress Report No. 71, Research Laboratory of Electronics, M. I. T., October 15, 1963, pp. 122-130.
2. R. J. Briggs, Electron-Stream Interaction with Plasmas (The M. I. T. Press, Cambridge, Mass., 1964), Chap. 2.
3. Ya. B. Fainberg, V. I. Kurilko, and V. D. Shapiro, "Instabilities in the Interactions of Charged Particle Beams with Plasma," Soviet Phys. – Tech Phys. 6, 459-463 (1961).
4. R. J. Briggs, op. cit., see Appendix A.
5. P. M. Morse and H. Feshbach, Methods of Theoretical Physics (McGraw-Hill Book Company, Inc., New York, 1953), p. 437.

5. DYNAMICS OF THE PLASMA BOUNDARY

Introduction

We have presented elsewhere[1,2] charge-sheet trajectories for oscillations in an initially cold plasma slab. In this report we investigate the properties of a plasma slab in which the electrons have nonzero temperature. A self-consistent steady-state solution for the electron density is derived and the variation of the density profile with temperature is shown. The charge-sheet model is then used to study the electron dynamics resulting from an excitation of this self-consistent unperturbed state.

Unperturbed Electron Density Distribution

We assume that the ions are immobile and have a given density distribution $n_i(x)$, which (see Fig. IX-28) is zero outside some point $x = d$. The distribution is symmetric with respect to $x = 0$, and thus we are only concerned with the region $x > 0$. A

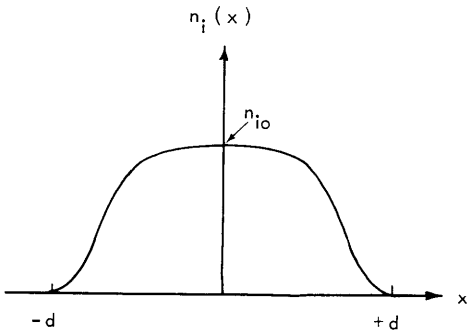

Fig. IX-28. Ion density for the plasma slab.

self-consistent unperturbed solution for the electron density distribution can be derived from the one-dimensional, time-independent, collisionless Boltzmann equation

$$v \frac{\partial f}{\partial x} - \frac{q}{m} E \frac{\partial f}{\partial v} = 0, \tag{1}$$

together with Poisson's equation

$$\frac{d^2\phi}{dx^2} = -\frac{q}{\epsilon_o}\left[n_i(x) - n_e(x)\right]. \tag{2}$$

The electric field is related to the potential $\phi(x)$ by

$$E = -\frac{d\phi}{dx}. \tag{3}$$

In Eq. 1, $f = f(v,x)$ is the electron distribution function, q is the magnitude of charge

on an electron, and m is the mass of an electron. The electron number density $n_e(x)$ is related to the distribution function $f(v,x)$ by an integral over velocities,

$$n_e(x) = \int_{-\infty}^{+\infty} f(v,x)\, dv. \tag{4}$$

If the electrons have a constant temperature T, a solution of (1) and (3) is

$$f(v,x) = A\, e^{-mv^2/2kT}\, e^{q\phi(x)/kT}, \tag{5}$$

where k is Boltzmann's constant, and A is a normalization constant. The electron density (from Eq. 4) is

$$n_e(x) = A\sqrt{2\pi kT/m}\; e^{q\phi(x)/kT}. \tag{6}$$

Thus Poisson's equation (2) reduces to

$$\frac{d^2\phi}{dx^2} = -\frac{q}{\epsilon_o}\left[n_i(x) - A\sqrt{2\pi kT/m}\; e^{q\phi(x)/kT}\right] \tag{7}$$

which must be solved for the potential $\phi(x)$ before the electron density can be found from (6). For a neutral one-dimensional plasma, the electric field must vanish at $x = \infty$. Hence

$$\frac{d\phi}{dx}(x=\infty) = 0. \tag{8}$$

By symmetry, for the neutral plasma, the electric field must vanish at $x = 0$,

$$\frac{d\phi}{dx}(x=0) = 0. \tag{9}$$

Since the electron density must also vanish at $x = \infty$, from Eq. 6, we have another condition on (7):

$$\phi(x=\infty) = -\infty. \tag{10}$$

Finally, since the electrostatic potential is arbitrary within a constant, we take $\phi(x=0) = 0$. Hence in Eq. 6 we define the electron density at $x = 0$ as $n_{eo} = A\sqrt{2\pi kT/m}$. The density for other values of x becomes

$$n_e(x) = n_{eo}\, e^{q\phi(x)/kT} \tag{11}$$

and Poisson's equation (7) may be written

$$\frac{d^2\phi}{dx^2} = -\frac{q}{\epsilon_o}\left[n_i(x) - n_{eo}\, e^{q\phi(x)/kT}\right]. \tag{12}$$

If the ion density vanishes at x = d, the matching conditions are that ϕ and $\frac{d\phi}{dx}$ are continuous at x = d.

We now wish to introduce normalized variables before solving Eq. 12. Assume that the ion density is given by

$$\begin{aligned} n_i(x) &= n_{io} f(x) \\ f(0) &= 1 \end{aligned} \tag{13}$$

so that n_{io} is the ion density at x = 0. The normalized potential $\xi(x)$ is defined by

$$\xi(x) = \frac{q\phi(x)}{kT}, \tag{14}$$

and a Debye length is assumed

$$\lambda_{Do}^2 = \frac{\epsilon_o kT}{q^2 n_{io}}. \tag{15}$$

All distances are measured in terms of this Debye length,

$$X = \frac{x}{\lambda_{Do}}. \tag{16}$$

In particular, the position of the ion boundary is given by

$$W = \frac{d}{\lambda_{Do}}. \tag{17}$$

If the ratio of electron density to ion density at X = 0 is called R_o,

$$R_o = \frac{n_{eo}}{n_{io}}, \tag{18}$$

Eq. 12 becomes

$$\frac{d^2\xi}{dX^2} = -f(X) + R_o\, e^{\xi(X)}. \tag{19}$$

An explicit solution to (19) may be obtained as follows for the region outside the ion background where f = 0. Here (19) reduces to

$$\frac{d^2\xi}{dX^2} = R_o\, e^{\xi} \qquad X > W. \tag{20}$$

We make the substitution $p = \frac{d\xi}{dX}$, $\frac{d^2\xi}{dX^2} = p\frac{dp}{d\xi}$ and

$$p\frac{dp}{d\xi} = R_o e^{\xi} \tag{21}$$

so that

$$\frac{1}{2}p^2 = R_o e^{\xi} + C_1. \tag{22}$$

From Eqs. 8 and 10 we deduce that $C_1 = 0$. For $X > W$, we then have

$$\frac{d\xi}{dX} = -\sqrt{2R_o}\, e^{\frac{1}{2}\xi}. \tag{23}$$

This equation can be integrated to give

$$e^{\xi} = \frac{2}{R_o(X+C_2)^2}, \tag{24}$$

where C_2 is the constant of integration. If the electron density at $X = W$ is n_{ew}, the density for $X > W$ is given by

$$\frac{n_e(X)}{n_{io}} = \frac{2}{\left(X - W + \sqrt{\frac{2n_{io}}{n_{ew}}}\right)^2} \qquad X > W. \tag{25}$$

Equation 25 shows that the electron density is inversely proportional to X^2 for $x > W$, independent of the value of ion density for $X < W$.

In order to find the electron density for $X < W$, Eq. 19 must be integrated numerically, in general. The procedure is to start at $X = 0$ with the conditions $\xi(0) = 0$ and $\frac{d\xi}{dX} = 0$. Since R_o is not known, a guess is made. From (23), since ξ and $\frac{d\xi}{dX}$ are continuous at $X = W$, the following condition is a constraint on the numerical solution:

$$\frac{d\xi}{dX} + \sqrt{2R_o}\, e^{\frac{1}{2}\xi} = 0 \qquad X = W. \tag{26}$$

The left side of (26) is calculated and the value is compared with 0. If it is not 0, R_o is changed and (19) is again integrated to $X = W$ and the constraint of (26) is checked. This is repeated until an R_o that satisfies (26) is found. Then the density can be found from (19) for $X < W$ and from (25) for $X > W$.

Rectangular Ion Distribution

We consider the special case in which the ions are uniformly distributed between X = 0 and X = W, so

$$f(X) = 1 \qquad 0 < X < W. \tag{27}$$

In this case, Eq. 19 becomes

$$\frac{d^2\xi}{dX^2} = -1 + R_o\, e^{\xi}. \tag{28}$$

Making the same substitutions as in the solution to Eq. 20, we find

$$\frac{1}{2}\left(\frac{d\xi}{dX}\right)^2 = R_o\, e^{\xi} - \xi + C_3. \tag{29}$$

By using $\frac{d\xi}{dX}(X=0) = 0$ and $\xi(0) = 0$, the constant C_3 may be evaluated as $C_3 = -R_o$. Hence,

$$\frac{d\xi}{dX} = -\sqrt{2}\,\sqrt{R_o(e^{\xi}-1) - \xi} \qquad X < W. \tag{30}$$

This equation is integrated once more to yield an implicit expression for ξ:

$$X = -\int_0^{\xi} \frac{d\xi'}{\sqrt{2}\,\sqrt{R_o(e^{\xi'}-1) - \xi'}} \qquad X < W. \tag{31}$$

Again, R_o is still unknown. In this case we may obtain R_o by matching $\xi(0)$ and $\frac{d\xi}{dX}$ at X = W, and then using (30) and (23), which gives

$$\xi(W) = -R_o. \tag{32}$$

When (32) is used with (31) an integral equation for R_o results:

$$W + \int_0^{-R_o} \frac{d\xi'}{\sqrt{2}\,\sqrt{R_o(e^{\xi'}-1) - \xi'}} = 0. \tag{33}$$

Thus, for a given value of $W = \frac{d}{\lambda_{Do}}$, Eq. 33 must be solved for $R_o = \frac{n_{eo}}{n_{io}}$. Equation 31 can then be used to find $\xi = \xi(X)$ implicitly up to X = W. The electron density is found from

$$\frac{n_e(X)}{n_{io}} = R_o\, e^{\xi(X)} = \frac{n_{eo}}{n_{io}}\, e^{\xi}. \tag{34}$$

From (32) and (34), we see that the electron density at the ion boundary X = W is

$$\frac{n_e(W)}{n_{io}} = \frac{n_{eW}}{n_{io}} = R_o\, e^{-R_o}, \tag{35}$$

and thus the electron distribution for X > W can now be found from Eq. 25.

Numerical Results for Rectangular Ion Distribution

We have integrated Eq. 19, subject to the constraint of Eq. 26, for the case of a uniform ion distribution with a sharp edge at X = W. The numerical method used

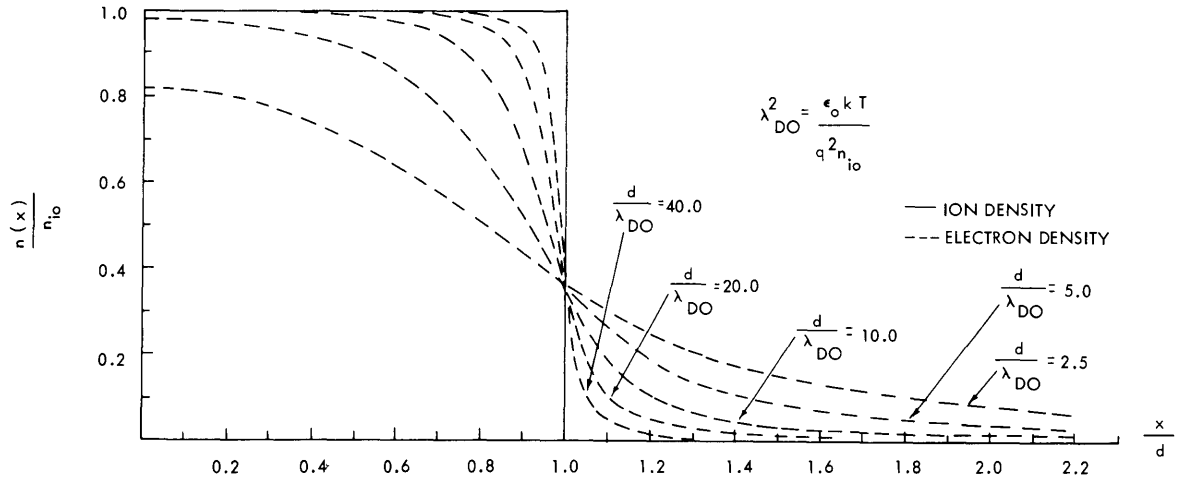

Fig. IX-29. Electron density as a function of electron temperature.

was the Runge-Kutta method for integrating the differential equation and then the method of variable secant[3] on Eq. 26 to find each successive new guess for R_o. The results are shown in Fig. IX-29 for several values of $W = d/\lambda_{Do}$. Note that for $d/\lambda_{Do} > 10$ the electron density follows the ion density very closely and drops off sharply outside the ion background.

The computations shown in Fig. IX-29 were checked by using the alternative method described above for the rectangular ion distribution. In this case the integral equation (33) was solved for R_o by Newton's method and (31) was used to compute the density for X < W.

Note that all of the electron density plots in Fig. IX-29 appear to go through the same point (0.37) at the ion boundary, x = d. This occurs because the electron density at the boundary is $R_o\, e^{-R_o}$. The value of R_o drops only to ~0.82 for $d/\lambda_{Do} = 2.5$, so that the density at the edge is $0.82\, e^{-0.82} = 0.361$. In the limit of a cold plasma, $R_o = 1$

and the density at the boundary is $e^{-1} = 0.368$. On the scale shown in Fig. IX-29 the difference between these points cannot be seen.

Charge-Sheet Model for the Hot Plasma

The plasma charge density will now be divided into electron and ion charge sheets.[1,2] The ion sheets are distributed uniformly between x = -d and x = +d and are immobile. The electron sheets all have the same charge but are given a spacing that is inversely

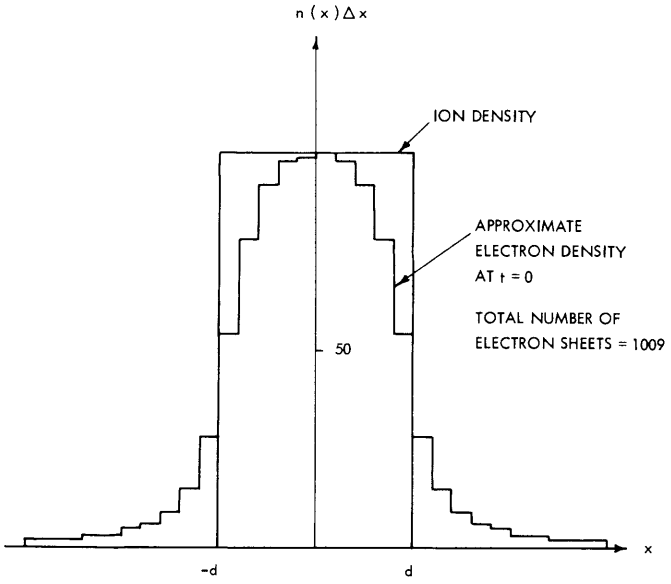

Fig. IX-30. Electron density at t = 0 for $d/\lambda_{Do} = 5.0$.

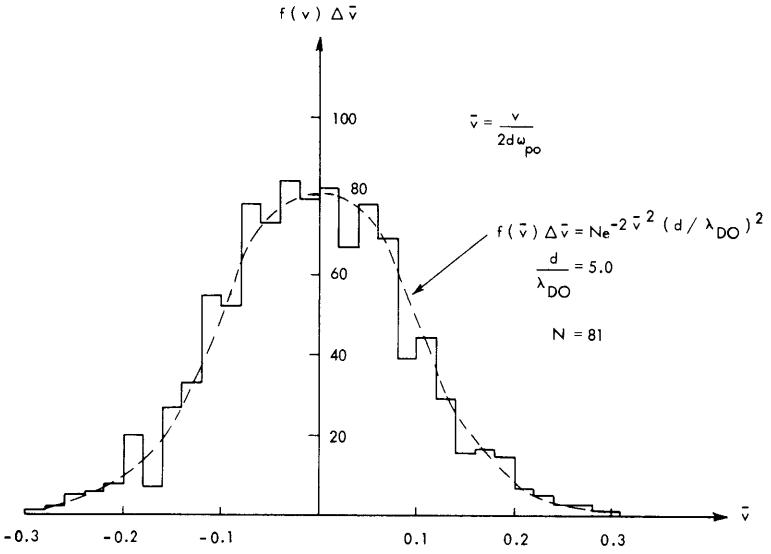

Fig. IX-31. Velocity distribution of electrons at t = 0 for $d/\lambda_{Do} = 5.0$.

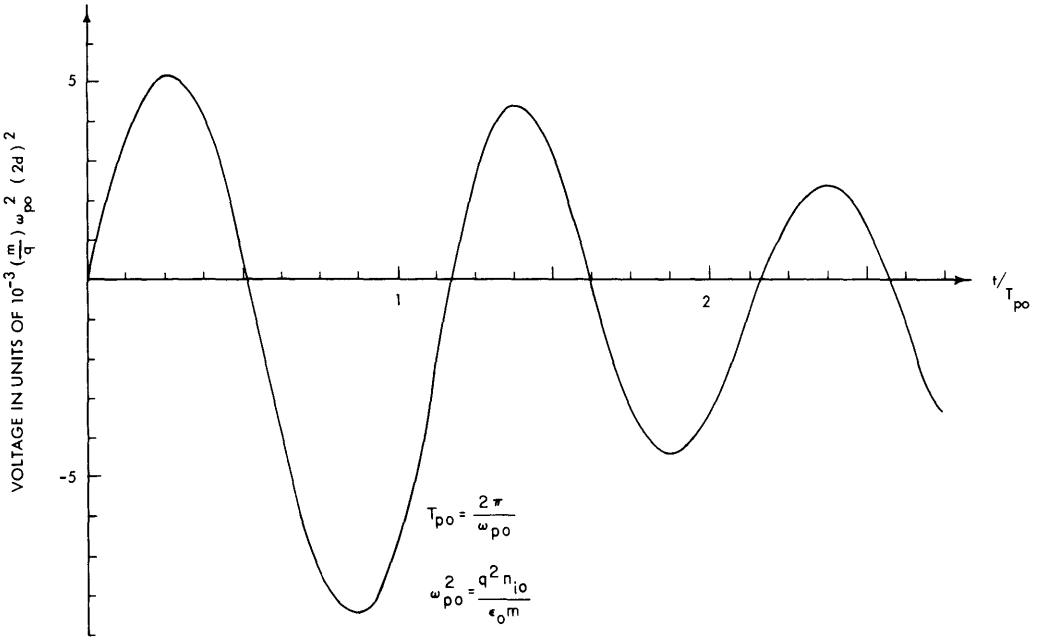

Fig. IX-32. Voltage as a function of time for $d/\lambda_{Do} = 5.0$.

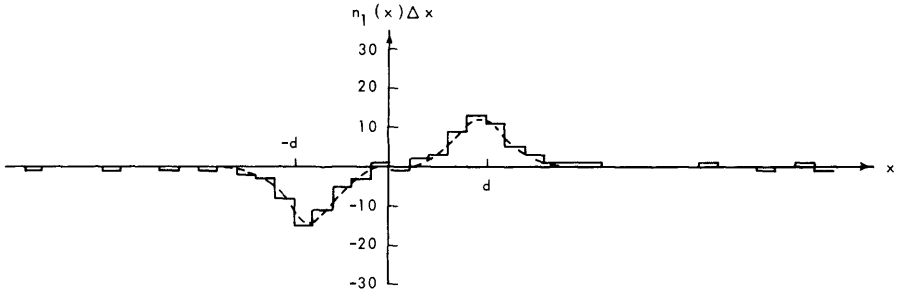

Fig. IX-33. Initial density perturbation.

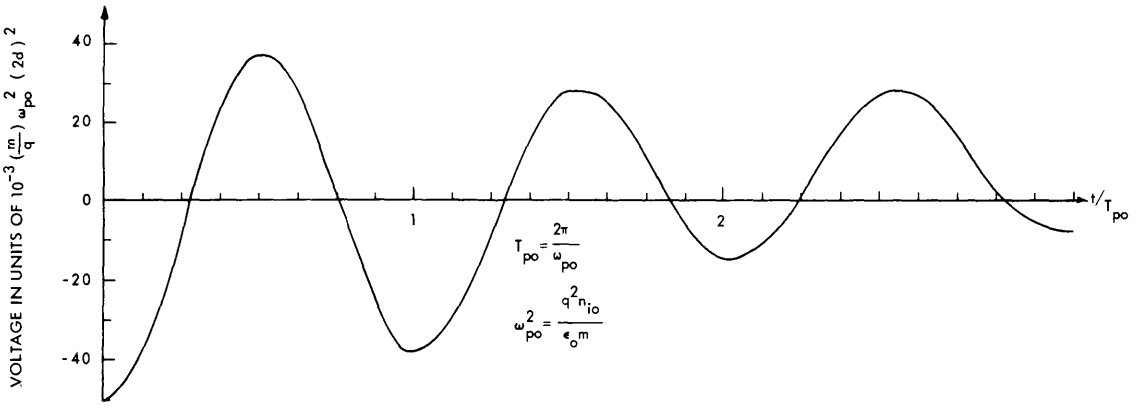

Fig. IX-34. Voltage for the density perturbation shown in Fig. IX-33.

proportional to the unperturbed state density distributions shown in Fig. IX-29. The velocity of each electron sheet is chosen by means of a random number table to generate a Maxwellian distribution in velocities as given in Eq. 5.

Preliminary results have been obtained for the case $d/\lambda_{Do} = 5.0$. The initial density distribution is shown in Fig. IX-30. The velocity distribution as chosen by the random number generator is given in Fig. IX-31.

To calculate the dynamics of the electrons for $t > 0$, an approximate method with fixed time steps has been used.[4] This method accounts for single-sheet crossings in an average sense over a time step.

In order to check the unperturbed state, the dynamics of the electrons distributed as shown in Figs. IX-30 and IX-31 were found. The voltage across the slab was calculated and is shown in Fig. IX-32. An oscillation has clearly been excited in what was to have been an unperturbed equilibrium state. We have found that this oscillation is generated by a current that exists at $t = 0$. The velocity distribution shown in Fig. IX-31 does not have a zero average value; in fact, the average velocity is approximately 4 per cent of the thermal velocity.

Finally, we have excited an oscillation in this plasma by giving all of the electron sheets a uniform displacement at $t = 0$. The displacement chosen was $\delta = .025\ d$, and this leads to a perturbation charge density at $t = 0$ as shown in Fig. IX-33. The electron dynamics for this initial perturbation give the voltage shown in Fig. IX-34 for $t > 0$.

The present work will be extended to study the dependence of the oscillations in the hot plasma slab on temperature and the type of initial perturbation given to the electrons.

H. M. Schneider

References

1. H. M. Schneider, Phys. Fluids 9, 2299 (1966).
2. H. M. Schneider, Quarterly Progress Report No. 84, Research Laboratory of Electronics, M.I.T., January 15, 1967, pp. 149-151.
3. C. E. Fröberg, Introduction to Numerical Analysis (Addison-Wesley Publishing Company, Inc., Reading, Mass., 1965).
4. M. R. Feix, G. A. Massel, and R. H. Weinstein, "Computer Experiments on the Microscopic Theory of Plasmas," NASA Report SP-153.

6. INTERACTIONS OF A SPIRALING ELECTRON BEAM WITH A PLASMA

In an attempt to understand some of the effects observed in the spiraling electron beam-plasma experiment[1,2] a theoretical analysis of related beam-plasma models has been started. We have performed rigid-beam analyses in the electrostatic limit as outlined by Bers.[3] These solutions are valid when the wavelength is large compared with the beam thickness. This technique of rigid beam displacement has also been used in the study of relativistic accelerator beams.[4] Some of the results of this analysis are described in this report.

Infinite Rigid Beam

Consider an infinite, uniform fluid of electrons (neutralized by infinitely massive ions) streaming across the magnetic field with velocity v_o. (See Fig. IX-35.) This

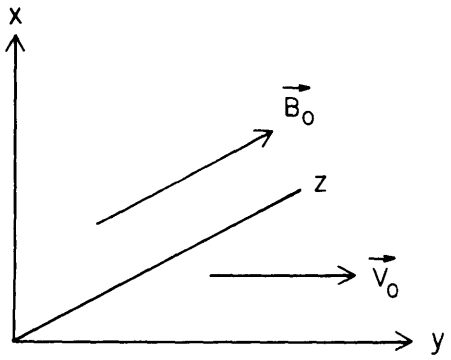

Fig. IX-35. Geometry of an infinite beam with motion across the magnetic field.

zero-order motion can result from an applied electric field. The electrostatic limit is assumed, and $\bar{\delta}_1$ is the first-order perturbation of the beam electrons, which is assumed to be a function of y and the frequency ω only, and has components in the x and y directions.

$$\bar{\delta}_1 = (\bar{i}_x \delta_x + \bar{i}_y \delta_y)\, e^{j(\omega t - \beta y)}.$$

The first-order equation of motion can be written

$$m_o n_o \frac{d^2}{dt^2} \bar{\delta}_1 = e n_o \left(-\nabla \phi_1 + \frac{d}{dt} \bar{\delta}_1 \times \bar{B}_o\right), \tag{1}$$

where m_o is the electron mass; n_o, the electron density; e, the electron charge; and ϕ_1, the first-order electric potential. Poisson's equation can be written

$$\nabla^2 \phi_1 = \frac{e}{\epsilon_o} n_o \nabla \cdot \bar{\delta}_1. \tag{2}$$

Combining Eqs. 1 and 2 gives the dispersion relation

$$\Omega^2\left(\Omega^2-\omega_{pe}^2-\omega_{ce}^2\right) = 0, \tag{3}$$

where

$$\Omega = \omega - \beta v_o$$

$$\omega_{pe}^2 = \frac{e^2 n_o}{\epsilon_o m_o}$$

$$\omega_{ce} = \frac{eB_o}{m_o}.$$

A plot of this dispersion relation is shown in Fig. IX-36. The two waves $\Omega^2 = 0$ are labeled synchronous waves. These waves correspond to a DC displacement of the beam

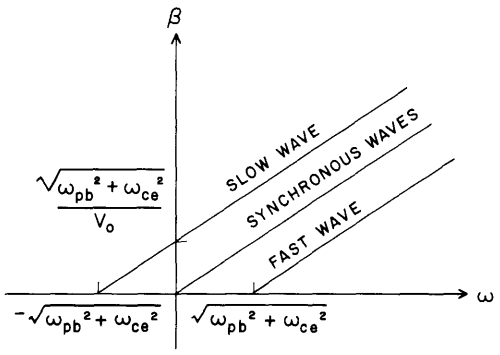

Fig. IX-36.
Dispersion relation for a rigid infinite beam moving across the magnetic field.

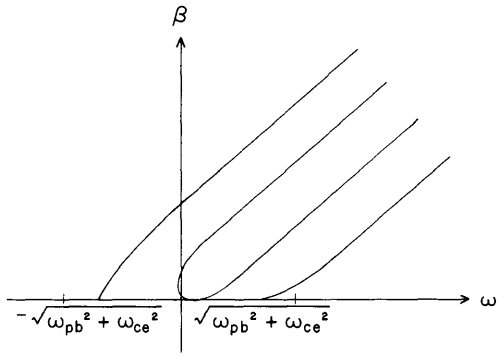

Fig. IX-37.
Dispersion relation for a strip beam moving across the magnetic field.

particles in the x direction. There is no first-order bunching or electric field. The waves labeled fast and slow are associated with elliptical motion of the beam particles.

Rigid Strip Beam

If it is assumed that the unperturbed beam density varies with x, a solution can be obtained for the beam waves in the following manner. The force equation now becomes

$$m_o n_o(x) \frac{d^2}{dt^2}\bar{\delta}_1 = e\, n_o(x)\left[-\nabla\phi_1(x) + \frac{d}{dt}\bar{\delta}_1 \times \bar{B}_o\right]. \tag{4}$$

Poisson's equation becomes

$$\nabla^2\phi_1(x) = \frac{e}{\epsilon_o}\left[n_o(x)\,\nabla\cdot\bar{\delta}_1 + \bar{\delta}_1\cdot\nabla n_o(x)\right]. \tag{5}$$

Again, we assume that the first-order quantities vary as

$$e^{j(\omega t-\beta y)}.$$

While there is an x-dependence in n_o and ϕ_1, $\bar{\delta}_1$ is assumed to be independent of x.

We next define an averaging operator as

$$\langle\ \rangle \equiv \frac{1}{\tau}\int_{-\infty}^{\infty} dx,$$

where τ is a characteristic beam thickness. Taking this average of every term in Eq. 4 removes the x-dependence and gives

$$\frac{d^2}{dt^2}\bar{\delta}_1 = -\frac{e\langle n_o\nabla\phi\rangle}{m_o\langle n_o\rangle} + \frac{e}{m_o}\frac{d}{dt}\bar{\delta}_1\times\bar{B}_o. \tag{6}$$

The assumptions

$$\phi_1(x) = \frac{1}{\sqrt{2\pi}}\int_{-\infty}^{\infty}\Phi_k\, e^{-jkx}\,dk$$

and

$$n_o(x) = \frac{1}{\sqrt{2\pi}}\int_{-\infty}^{\infty} N_k\, e^{-jkx}\,dk,$$

together with Poisson's equation yield

$$\Phi_k = j\frac{eN_k}{\epsilon_o}\frac{k\delta_x+\beta\delta_y}{k^2+\beta^2}.$$

With this expression for Φ_k, the averages of the force equation (6) can be expressed as follows:

$$\langle n_o\phi_1\rangle = j\frac{\beta\delta_y}{\epsilon_o\tau}e\int_{-\infty}^{\infty}dk\,\frac{N_kN_{-k}}{k^2+\beta^2} \tag{7}$$

and

$$\left\langle n_o\frac{\partial}{\partial_x}\phi_1\right\rangle = \frac{e\delta_x}{\epsilon_o\tau}\int_{-\infty}^{\infty}dk\,\frac{N_kN_{-k}k^2}{k^2+\beta^2}. \tag{8}$$

Given $n_o(x)$, N_k is known. Equations 7 and 8 combine with Eq. 6 to give the following dispersion relation

$$\left(\Omega^2-\omega_a^2\right)\left(\Omega^2-\omega_b^2\right) = \Omega^2\omega_{ce}^2, \tag{9}$$

where

$$\omega_a^2 = \frac{e^2\beta^2}{\epsilon_o m_o \langle n_o \rangle \tau}\int_{-\infty}^{\infty} dk\, \frac{N_k N_{-k}}{k^2+\beta^2}$$

and

$$\omega_b^2 = \frac{e^2}{\epsilon_o m_o \langle n_o \rangle \tau}\int_{-\infty}^{\infty} dk \frac{N_k N_{-k} k^2}{k^2+\beta^2}.$$

If one takes for $n_o(x)$ a Gaussian,

$$n_o(x) = \frac{\rho_o}{\tau\sqrt{\pi}}\, e^{-x^2/\tau^2},$$

the integrals for ω_a^2 and ω_b^2 can be carried out to give well-known functions.

A plot of the dispersion relation (9) for $n_o(x)$ a Gaussian is shown in Fig. IX-37. The synchronous beam waves of the infinite beam have split into a fast and a slow wave. For a fixed density, the amount of the split is determined by the beam thickness; the thinner the beam, the more the separation. The previous fast and slow waves are pulled in and intersect the ω axis at a frequency lower than the hybrid.

Rigid Strip Beam and Ion Plasma

If one wishes to analyze a strip beam like the one described above in the presence of a plasma, the only change, for propagation across the magnetic field, is the introduction of the effective plasma dielectric function, $K_\perp$, into Poisson's equation.

$$\nabla^2\phi_1 = \frac{e}{K_\perp \epsilon_o}\left(n_o \nabla\cdot\bar{\delta} + \bar{\delta}\cdot\nabla n_o\right).$$

The dispersion relation then becomes

$$\left(\Omega^2 - \frac{\omega_a^2}{K_\perp}\right)\left(\Omega^2 - \frac{\omega_b^2}{K_\perp}\right) = \Omega^2\omega_{ce}^2. \tag{10}$$

Since ω_a^2 and ω_b^2 are both proportional to the beam density, the limit of the dispersion

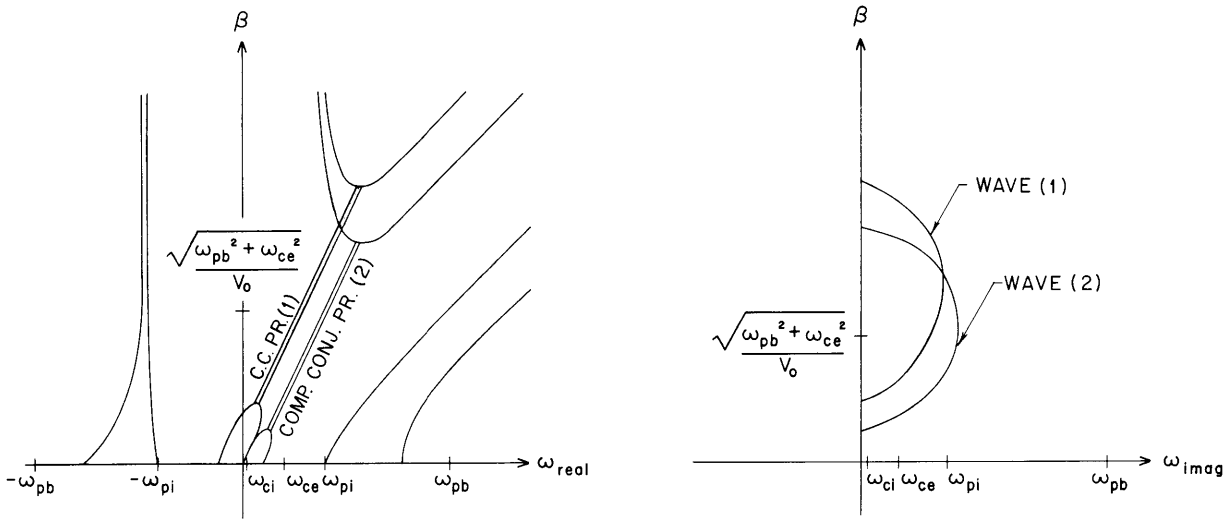

(a) REAL ω

(b) MAGNITUDE IMAGINARY ω

Fig. IX-38. Dispersion relation for a strip beam moving across B_o through an ion-plasma background, with $\omega_{ci} < \omega_{ce} < \omega_{pi} < \omega_{pb}$.

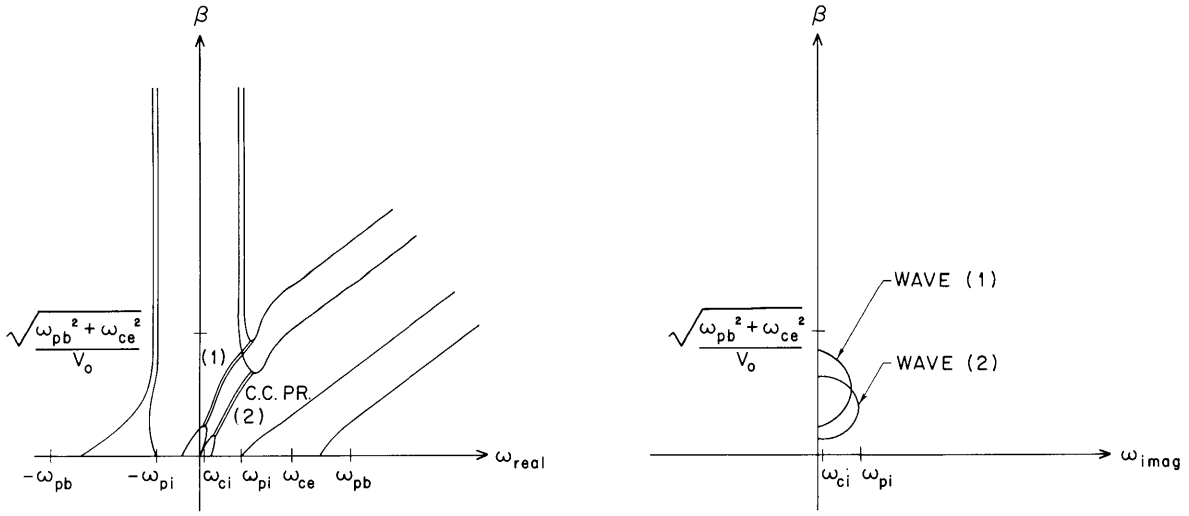

(a) REAL ω

(b) MAGNITUDE IMAGINARY ω

Fig. IX-39. Dispersion relation for a strip beam moving across B_o through an ion-plasma background, with $\omega_{ci} < \omega_{pi} < \omega_{ce} < \omega_{pb}$.

relation with no beam is simply

$$K_\perp^2 = 0$$

which gives the electrostatic plasma oscillations or waves across the magnetic field. As the plasma is removed, $K_\perp \to 1$ and Eq. 9 clearly goes to the strip-beam limit.

If the plasma is assumed to be made up of cold ions, then

$$K_\perp = 1 - \frac{\omega_{pi}^2}{\omega^2 - \omega_{ci}^2},$$

where ω_{pi} is the ion plasma frequency, and ω_{ci} is the ion cyclotron frequency. This expression for $K_\perp$ and the ω_a and ω_b expressions that result when a Gaussian is taken for the spatial electron density distribution were used to plot the dispersion relation. Real values were assumed for β, and the equation was then solved for ω.

Assuming $\omega_{ci} < \omega_{ce} < \omega_{pi} < \omega_{pb}$ gave the dispersion relation shown in Fig. IX-38. ω_{pb} is the electron plasma frequency in the center of the beam. For frequencies below ω_{pi} there is strong coupling. This appears to be a reactive-medium region where $K_\perp$ is negative. Above ω_{pi}, the plasma and beam waves uncouple.

Assuming $\omega_{ci} < \omega_{pi} < \omega_{ce} < \omega_{pe}$ causes the reactive-medium region to occur for a smaller frequency spread. This effect can be seen in Fig. IX-39.

We plan to extend this type of analysis to include beam velocities and wave propagation along the magnetic field.

B. Kusse

References

1. B. Kusse and A. Bers, "Cross-Field Beam Plasma Interactions," Quarterly Progress Report No. 82, Research Laboratory of Electronics, M. I. T., July 15, 1966, pp. 154-157.
2. B. Kusse and A. Bers, "Interaction of a Spiraling Electron Beam with a Plasma," Quarterly Progress Report No. 86, Research Laboratory of Electronics, M. I. T., July 15, 1967, pp. 154-156.
3. A. Bers, "Theory of Beam-Plasma Interactions," Quarterly Progress Report No. 85, Research Laboratory of Electronics, M. I. T., April 15, 1967, pp. 163-167.
4. S. Weinberg, "The Hose Instability Dispersion Relation," J. Math. Phys., Vol. 5, No. 10, pp. 1371-1386, October 1964.

7. "LOW-FIELD" MICROWAVE EMISSION FROM CONTACTLESS INDIUM ANTIMONIDE SAMPLES

Introduction

Broadband microwave emission from indium antimonide samples subjected to low electric and moderate magnetic fields has been observed by a number of workers,[1-4] since it was originally reported by Buchsbaum, Chynoweth, and Feldmann.[5] In a typical experiment, a single crystal of indium antimonide, with dimensions roughly $1 \times 1 \times 10$ mm^3, is mounted in a waveguide or coaxial microwave structure. Liquid nitrogen or liquid helium is used to cool the sample to a temperature near 77°K or 4.2°K. An electric field is applied along the longer dimension of the sample by passing a current through ohmic contacts located at each end. This current is usually pulsed to avoid heating the sample. A static magnetic field is applied at some angle from 0 to 90° with respect to the direction of current flow in the sample. Under these conditions, the sample emits microwave noise having a relatively flat spectrum, provided that the applied electric and magnetic fields exceed certain threshold values. Typical threshold electric and magnetic fields are 3-15 V/cm and 1000-4000 Gauss, with somewhat lower threshold magnetic fields occurring at 4.2°K.

A number of features of the emission may be noted. First, while the noise output from a sample is generally an increasing function of the applied electric and magnetic fields, particularly in the region near threshold, plots of output versus electric or magnetic field (made, respectively, with the magnetic or electric field held fixed) may show regions of saturation or decreasing output as the field magnitude is increased.[1,2,3,5] Also, certain particular combinations of electric and magnetic fields may produce exceptionally large noise outputs. This "spiking" is observed by sweeping the electric or magnetic field during the time when the electric field pulse is applied to the sample.[2,3] A still more complicated structure of the noise output as a function of magnetic field has recently been observed in experiments[5] conducted at 4.2°K. Next, maximum noise output ordinarily occurs when the applied electric and magnetic fields are parallel.[1,3,4] The emission may exceed that from a black body at 100,000°K, at S-band frequencies,[5] with somewhat less output at X-band. Finally, while the emission is generally unchanged by a reversal of the applied magnetic field,[1] the intensity of the emission may change considerably when the applied electric field is reversed.[3-5]

The low-field emission described here was observed from samples that had a wide variety of surface treatments and contact types. This apparent insensitivity of the emission to the surface conditions and contacting methods employed supported the contention that bulk processes rather than contact or surface effects were responsible for the emission. The rather large changes which sometimes occurred upon reversal of the applied electric field suggested, however, that contacts might play some role in the

generation of the emission. In order to determine whether the contacts were in fact necessary for production of the emission, the experiment described here was undertaken.

Development of the "Contactless Sample" Experiment

a. Basic Idea

It was apparent that contact effects could be completely and unequivocally eliminated from the experiment only by eliminating the contacts themselves. This could be done by making samples in the shape of a square ring, as shown in Fig. IX-40. The required

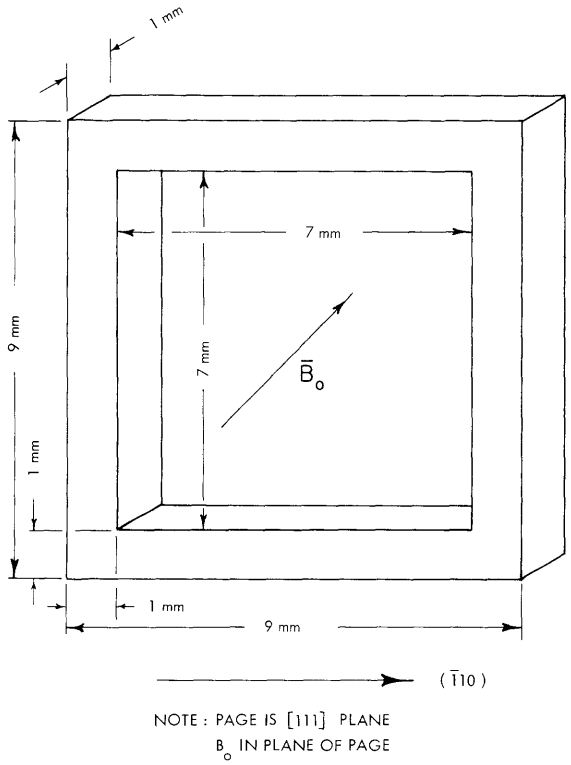

Fig. IX-40. Square ring sample used in the experiment.

electric field could then be induced in the sample by applying a time-variant magnetic field in the direction normal to the plane of the sample. A conventional electromagnet could supply the required static magnetic field, $\overline{B}_o$.

It was known that the transverse and longitudinal magnetoresistance effects in indium antimonide were quite different in magnitude, and that those sides of the sample which, through magnetoresistance effects, had larger resistance would absorb proportionately

more of the induced electric field. Accordingly, for the first series of experiments we decided to orient the static magnetic field along the diagonal of the square sample. This makes the magnitudes of the transverse and longitudinal magnetic fields applied to each leg of the square equal, and results in the same relative resistance change for all legs of the sample. No one leg of the sample is favored over another with respect to its share of the induced electric field.

A frequency of 20 MHz was selected for the time-variant magnetic field. This represented a compromise between the conflicting requirements of efficient RF coupling to the sample and penetration of the induced fields into the bulk of the sample. It was not known initially whether the pulsed DC electric field used in previous experiments[1-5] could be replaced by a sinusoidal burst at 20 MHz. Accordingly, we conducted a preliminary experiment designed to test the effectiveness of a radiofrequency pulse in producing the microwave emission.

b. Preliminary Test

A rod of N-type single-crystal indium antimonide, with dimensions roughly $0.4 \times 0.4 \times 7$ mm^3, was mounted midway between the short sides of an X-band waveguide. The axis of the rod was aligned parallel to the microwave electric field of the TE_{10} waveguide mode. Electron density and mobility at 77°K were 10^{14} per cm^3 and 6×10^5 cm^2/V-sec, respectively. The orientation of the sample with respect to the crystal axes was not determined. The sample and waveguide structure were immersed in liquid nitrogen contained in a dewar flask to maintain a sample temperature of 77°K. Either DC or radiofrequency electric field pulses could be applied to the sample through ohmic contacts at each end. A static magnetic field was applied at an angle of 45° with respect to the rod axis so that conditions in the bulk of the sample would be similar to those in each leg of the square "contactless" sample. Microwave emission from the sample was detected with an X-band radiometer.

Figure IX-41 shows a plot of noise output versus applied electric field at constant magnetic field. The frequency of observation was 9.5 GHz. Three cases are shown: positive pulsed DC electric field, negative pulsed DC electric field, and pulsed 20 MHz electric field. The magnitude of the emission changed with reversal of the electric field, as was reported previously.[3-5] More important to the work at hand, however, was the fact that the observed emission was roughly of the same order of intensity for a given peak electric field, whether this peak occurred in a sinusoidal burst or in a DC pulse. This result was not extremely surprising, since electron collision frequencies in indium antimonide are much greater than 20 MHz, so that essentially steady-state conduction processes prevail at all times. It did, however, show that the rise time of the process producing the emission was less than one half of one period at 20 MHz, and that the emission should be

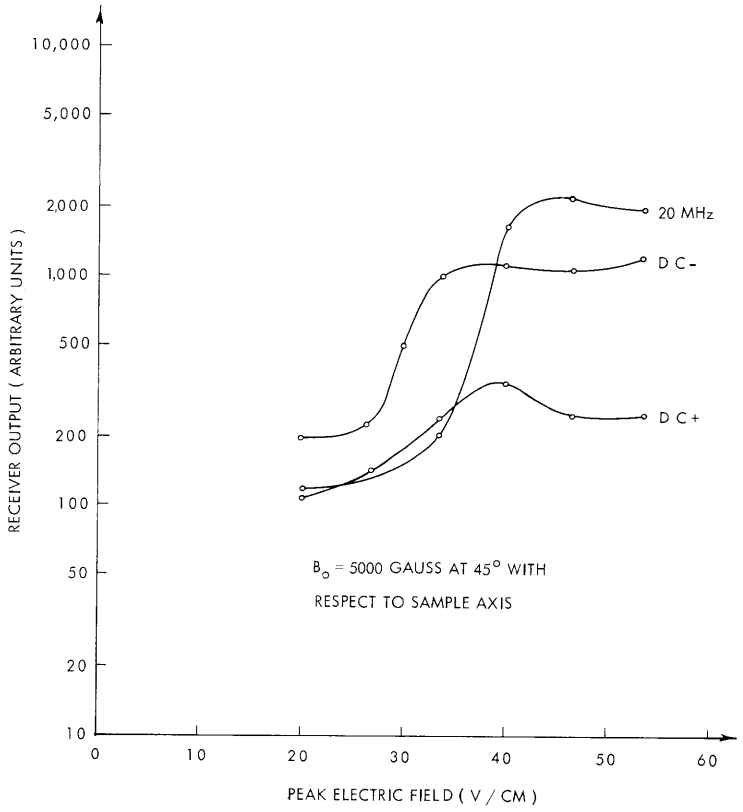

Fig. IX-41. Microwave emission from a rod-shaped sample as a function of peak electric field for 3 different electric field conditions. Frequency of observation, 9.5 gHz; electric field pulse duration; 30 μsec; pulse repetition rate, 300 pps. Divide output values by 2.25 for direct comparison with Fig. IX-45.

observed from the contactless sample if only bulk processes were involved.

c. Arrangement for the "Contactless" Experiment

Figure IX-40 shows the square-ring sample used in the experiment, with pertinent dimensions. The sample was fabricated from a single crystal of N-type indium antimonide. The plane of the sample coincides with the [111] crystallographic plane, and one edge of the square lies along the $(\bar{1}10)$ crystal axis. Electron density and mobility are 10^{14} per cm^3, and 6×10^5 cm^2/V-sec at 77°K, respectively. The DC resistance around the ring is ~40 Ohms at 77°K with no magnetic field applied, and may increase to 2 or 3 times this value when the applied magnetic field reaches 6 kG.

The sample was cut from an indium antimonide disc, 1 mm thick, by using a wire saw. The center hole was made by sandblasting, and was finished to final dimensions by manual lapping. Because of these primitive fabrication techniques, the sample shape was somewhat irregular. The sample surface was treated with a bromine-methanol

etch after lapping.

The sample was mounted in an X-band waveguide as shown in Fig. IX-42. The plane of the sample coincided with the plane of the TE_{10} mode electric field. The off-center mounting position was chosen to avoid the possibility of mutual cancellation of the waves

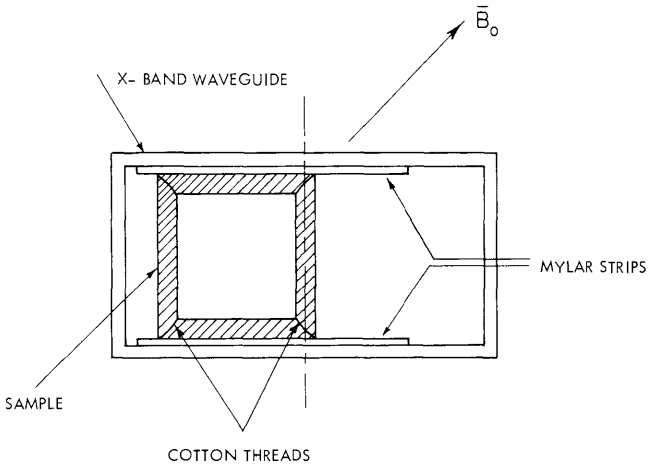

Fig. IX-42.
Mounting of the "contactless" sample – view looking into one end of the waveguide.

excited in the waveguide by those sides of the square parallel to the dominant mode electric field. The sample was supported by thin (5 mil) mylar sheets to which it was secured with cotton thread. Since the mylar sheet retained its flexibility even at 77°K, the sample was not unduly stressed during the extreme temperature cycles to which it was subjected.

Figure IX-43 shows an external view of the waveguide and RF magnetic field

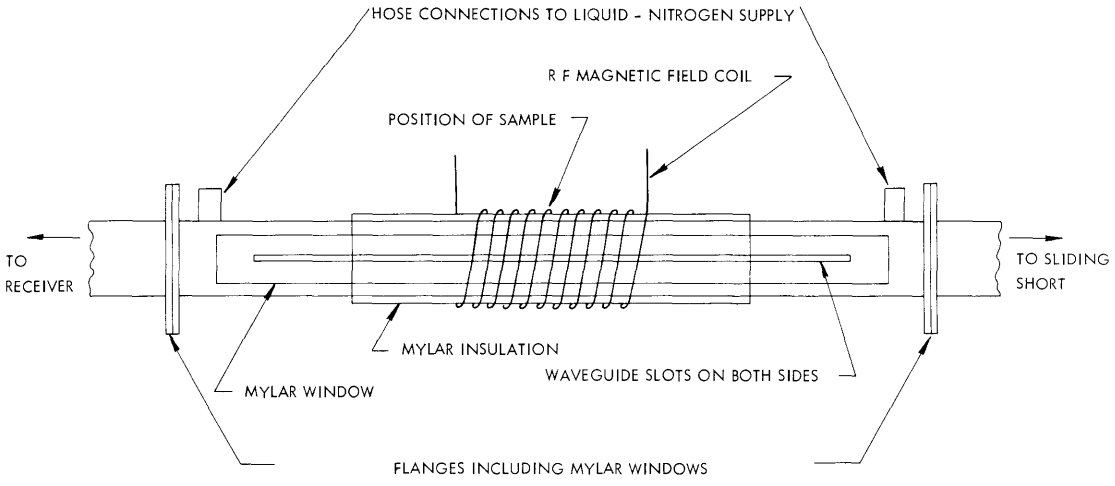

Fig. IX-43. View of the waveguide and RF magnetic field coil system.

structure in which the sample was mounted. The waveguide was made of stainless steel to reduce heat conduction into the system, and was copper-plated to reduce RF losses. Slots, 8 inches long, were made along the centers of the broad faces of the waveguide to allow penetration of the RF magnetic field into the waveguide interior. The section of waveguide between the flanges was made fluid-tight by means of mylar windows, placed over the waveguide slots and across the waveguide at the flange positions. In ordinary operation, liquid nitrogen was allowed to flow into this section of the waveguide through the two tubes shown, thereby maintaining the sample temperature near 77°K. A sliding short was placed behind the sample for tuning purposes. In spite of all of the perturbations imposed on the waveguide structure by this sample mounting scheme, loss through the system when filled with liquid nitrogen measured less than 1 dB.

The RF magnetic field coil consists of 14 turns of No. 16 insulated solid copper wire wound on the waveguide structure. The coil is insulated from the waveguide by 8 layers of 5-mil mylar sheet wrapped around the waveguide beneath the winding. The coil inductance is approximately 2.2 μH, and when resonated at 20 MHz the coil exhibits a Q in excess of 100, provided the waveguide is filled with liquid nitrogen. High Q is particularly important in this system, since for a given input power and coil geometry the RF magnetic field that is produced is proportional to $Q^{1/2}$.

Figure IX-44 shows a schematic representation of the complete experimental system.

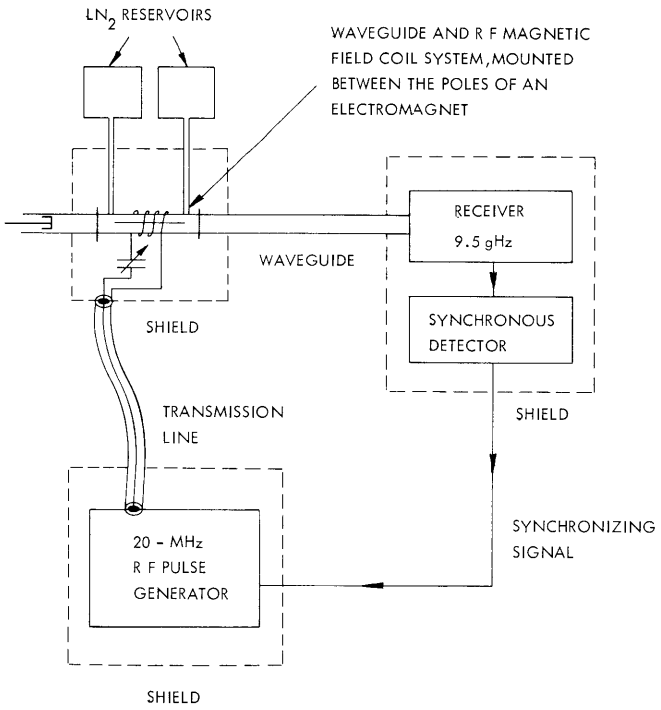

Fig. IX-44. Schematic representation of the experimental system.

The section of waveguide containing the sample is enclosed in a shielded box filled with chips of plastic foam to reduce heat flow to the sample. A vacuum variable capacitor placed inside this box is used to form a series-resonant circuit with the RF magnetic field coil. Pulses of 20 MHz radiofrequency energy are fed to the resonant circuit from an external generator. The RF generator is capable of supplying somewhat more than 12 kW peak envelope power to the 5-Ohm impedance presented by the tuned circuit at resonance. Output from the sample is carried by a waveguide to an X-band receiver which employs a synchronous detector. The receiver IF bandwidth is 10 MHz, and the over-all system noise figure is approximately 6 dB. Both the receiver and RF pulse generator are enclosed in RF-tight shields to reduce unwanted signal pickup.

Experimental Results

The results presented here are preliminary. They are, however, sufficient to establish that low-field emission can be produced from contactless samples.

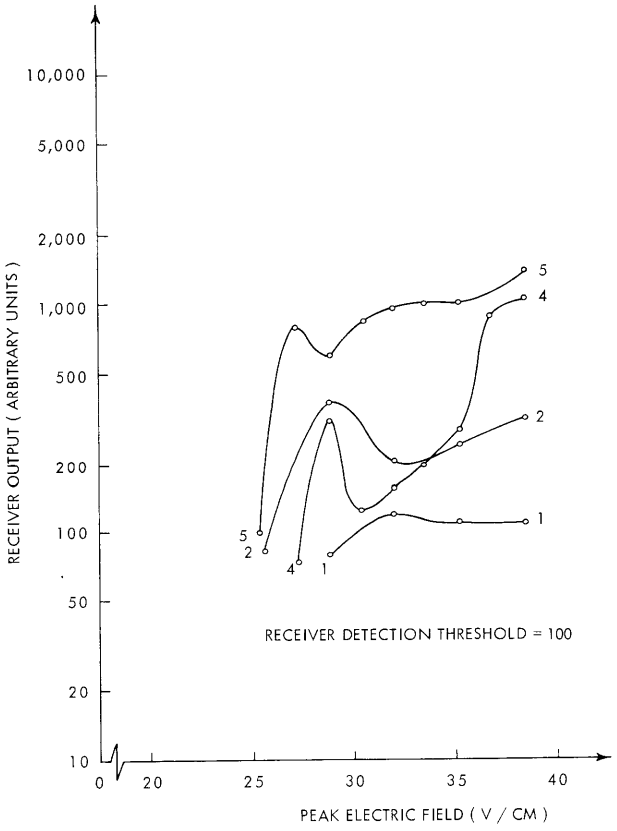

Fig. IX-45. Receiver output vs sample electric field at constant magnetic field. Frequency of observation, 9.5 gHz; pulse parameters, 20-μsec duration, 200 pps (curves 1, 2) and 80-μsec duration, 50 pps (curves 4, 5); magnetic field B_o: curve 1, 3175 Gauss; curve 2, 3620 Gauss; curve 4, 4080 Gauss; curve 5, 4900 Gauss.

Furthermore, the gross properties of the microwave emission are similar to those previously observed for rod-shaped samples having contacts at each end. Thus, while the contacts may modify the emission, it has been shown that they are not necessary for its production.

Figure IX-45 shows the microwave emission produced by the sample shown in Fig. IX-40 when operated in the system described in Figs. IX-43 and IX-44. The output is recorded as a function of peak electric field with constant magnetic field. The threshold electric and magnetic fields appear to be within the range reported by previous workers.[1-5] Peaks in the output may correspond either to the "spiking" previously observed[2,3] at 77°K or may be related to the peaks observed by Bekefi[5] at 4.2°K. The intensity of the observed emission is of the same order or stronger than that observed in our own preliminary tests. Results for different pulse lengths (Fig. IX-45) are directly comparable because the same very small duty factor was employed.

The electric field values must be considered approximate. They were inferred from search-coil measurements of the RF magnetic field which were valid only for samples of 50-Ohms resistance. Since the sample resistance may increase above 50 Ohms at higher static magnetic fields, thereby reducing the diamagnetic properties of the square ring, the electric field values are probably too low. Fortunately, the error introduced is in the form of a scale factor, which is constant for each magnetic field value. Preliminary measurements indicate that over the range of magnetic fields used the error is less than 30%.

Each pulse length that was used represents a compromise. With a 20-μsec RF pulse, the rise time of the RF magnetic field occupies almost half of the pulse length. The peak electric field induced in the sample is thus not constant during the pulse. The rise time is rather long, on account of the high Q of the RF magnetic field coil system. With 80-μsec pulses, the induced electric field is constant for most of the pulse duration. It appears, however, that sufficient heating of the sample occurs during the pulse to reduce the intensity of the microwave emission.

Future Work

The system now in use must be refined to make somewhat more accurate measurements. A variety of samples, sample positions in the waveguide, and orientations of the static magnetic field should also be used. More accurate calibrations of magnetoresistance effects will also be made.

Now that it has been shown that contacts are not, in fact, necessary for the production of low-field microwave emission from indium antimonide, theoretical studies of the problem, based on bulk interaction effects, can proceed with more confidence.

R. N. Wallace

References

1. S. J. Buchsbaum, A. J. Chynoweth, and W. L. Feldmann, J. Appl. Phys. 37, 2922 (1966).

2. T. Musha, F. Lindvall, and J. Hägglund, Appl. Phys. Letters 8, 157 (1966).

3. J. C. Eidson and G. S. Kino, Appl. Phys. Letters 8, 183 (1966).

4. G. Bekefi, A. Bers, and S. R. J. Bruech, Phys. Rev. Letters 19, 24 (1967).

5. S. J. Buchsbaum, A. J. Chynoweth, and W. L. Feldmann, Appl. Phys. Letters 6, 67 (1965).

IX. PLASMAS AND CONTROLLED NUCLEAR FUSION*

B. Applied Plasma Physics Related to Controlled Nuclear Fusion

Academic and Research Staff

Prof. D. J. Rose	Prof. L. M. Lidsky	Prof. S. Yip
Prof. T. H. Dupree	Prof. N. L. Oleson	Dr. K. Chung

Graduate Students

T. S. Brown	M. Hudis	D. H. Ross
K. R-S. Chen	M. Murakami	A. Sugawara
D. G. Colombant	G. R. Odette	C. E. Wagner
R. W. Flynn	L. C. Pittenger	A. Watanabe

1. HOLLOW-CATHODE ARC PLASMA

We are now engaged in three experimental programs on the hollow-cathode arc system (HCD): (i) Measurement of the radial flux by correlation techniques; (ii) Excitation of electrostatic plasma waves and measurement of real and imaginary parts of the propagation vector $K \rightarrow \vec{k}$; and (iii) Investigation of the decay process in the arc by temporarily removing the arc current.

This report presents some results obtained from the decaying plasma.

In order to temporarily remove the arc current, we used the circuit shown in Fig. IX-46. By activating the silicon-controlled rectifier, the current normally flowing

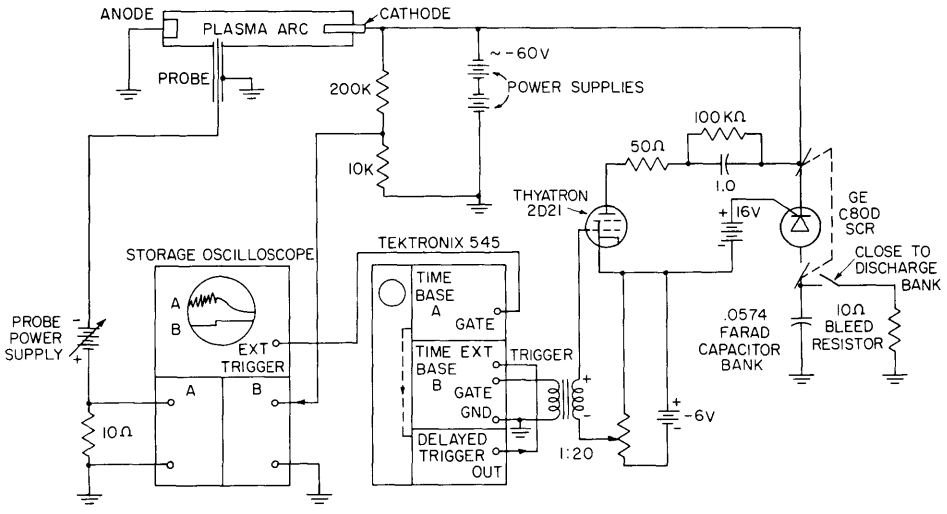

Fig. IX-46. Present circuit.

*This work was supported by the National Science Foundation (Grant GK-1165).

through the plasma is directed to the capacitor bank and the plasma starts to decay. We usually recover the normal arc after ≈50 msec, which is much larger than any decay time involved. The cathode's thermal inertia permits re-ignition of the arc. We used (a) electrostatic Langmuir probes to monitor local temperature and density decay processes as shown in Fig. IX-46, and (b) a 35-GHz microwave interferometer to measure the over-all density decay.

In Fig. IX-47a we show the ion saturation current of a probe located 1 cm from the axis. As we expected, the fluctuations[1] caused by the axial current die immediately

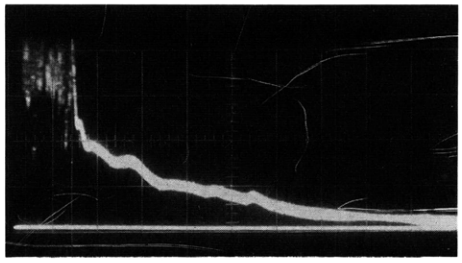

(a)

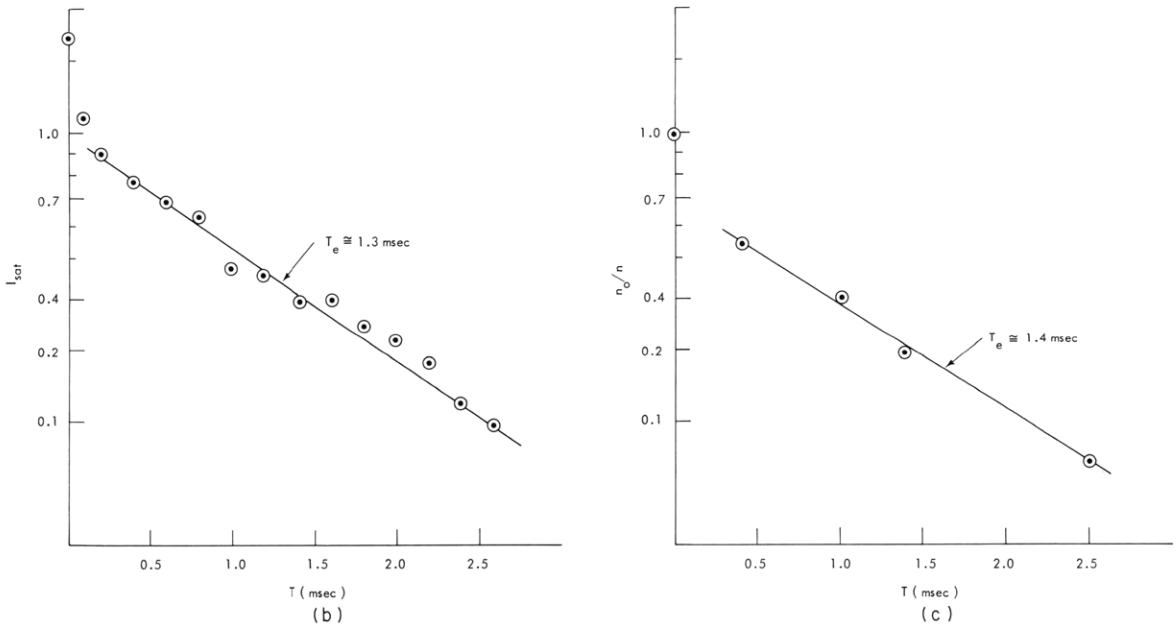

Fig. IX-47. (a) Illustrating ion saturation current of a probe 1-cm from the axis.
(b) Decay of ion saturation current of the arc plasma before the axial current was cut off. The plasma was unstable because of electrostatic ion cyclotron waves.
(c) Decay of the plasma density measured by a microwave interferometer. Conditions are the same as in (b).

after the axial current is cut off. Therefore the decaying plasma is very quiescent. This circumstance is very helpful for our wave propagation experiments. We have observed a propagating wave excited by a coarsely meshed probe, but that will not be reported at this time.

Figure IX-47b shows the Langmuir probe ion saturation current versus time, plotted semilogarithmically. We observe (apparently) that there is an initial fast decay (≈ 0.2 msec) followed by a subsequent slow decay (≈ 1.3 msec). The latter time is almost identical with that obtained from the microwave data (1.4 msec) shown in Fig. IX-47c. From all this, we might boldly conclude that there is an early rapid diffusion of hot plasma, plus decay of high-diffusion modes; then there would be an exponential decay of the plasma by pure diffusion in the fundamental mode, so that $n \propto \exp[-(t/\tau)]$.

Matters are not so simple. Figure IX-48 shows the identical data of Fig. IX-47b plotted as 1/n against t, in which case a straight line corresponds to recombination.

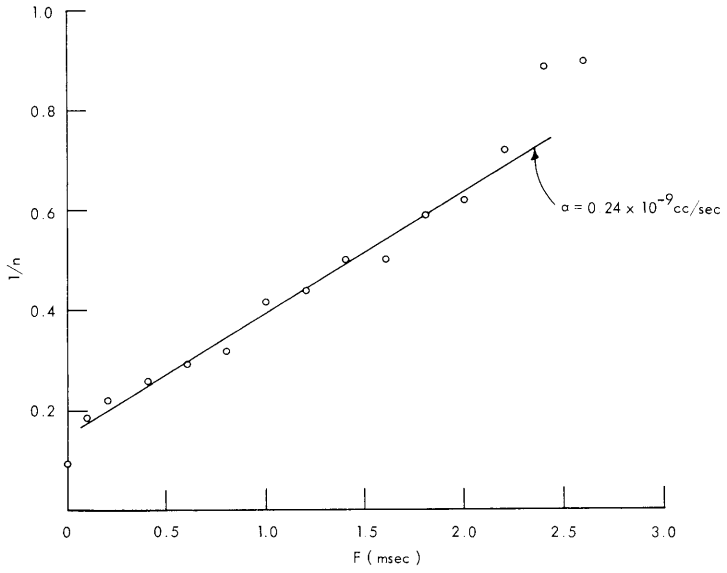

Fig. IX-48. Data of Fig. IX-47b plotted as 1/n against t.

The fit is fairly good, except at long time; the effective recombination coefficient would be $\alpha = 2.4 \times 10^{10}$ cm^3 sec^{-1}.

It is clear that density decay data over a more extended range are required so that we can properly see the roles of diffusion and recombination. Data are now being gathered over such an extended range.

As we have reported elsewhere,[1] our plasma column can be operated so that it exhibits (i) strong drift waves, (ii) predominant electrostatic ion cyclotron waves

or (iii) waves without any coherent oscillations. We are obtaining data of these three cases and measuring the initial and subsequent decay times. These data will be published in a future report.

D. H. Ross, K. Chung, D. J. Rose

References

1. K. Chung and D. J. Rose, Bull. Am. Phys. Soc. 12, 694 (1967).